Master's Degree in Astrophysics

2023-2024

GALAXY CLUSTER ENVIRONMENTAL QUENCHING IN COSMOLOGICAL SIMULATIONS

Aitor Larrañaga Jaio

Supervisors:

Andrea Negri
Claudio Dalla Vecchia

Resumen

La evolución de las galaxias es uno de los temas más significativos en la astrofísica moderna, y el impacto del entorno en dicha evolución es de vital importancia. Este trabajo se centra en el análisis de los procesos de apagado o de extinción ambiental (*environmental quenching*) que sufren las galaxias al caer en cúmulos galácticos, utilizando para ello simulaciones cosmológicas hidrodinámicas de última generación. El objetivo principal de este trabajo es comprender los mecanismos dominantes detrás del apagado ambiental dentro de los cúmulos y sus alrededores.

Para ello, se utilizan las 26 simulaciones de la muestra *Hydrangea*, los cuales pertenecen al proyecto C-EAGLE (Cluster-EAGLE), un conjunto de 30 simulaciones hidrodinámicas "*zoom-in*" centradas en cúmulos galácticos masivos en el rango de masa ($10^{14} < M_{200c}/\mathrm{M}_\odot < 10^{15.4}$). Estas simulaciones parten de las simulaciones MACSIS de solo materia oscura, y se resimulan con hidrodinámica y en alta resolución, abarcando diez radios viriales ($10 \times r_{200c}$) del cúmulo central en $z = 0$ y complementándolos con partículas de baja resolución más allá de esta región. En particular, estas simulaciones utilizan el código desarrollado para el proyecto EAGLE, y tienen una resolución de masa de $m_{\mathrm{gas}} = 1.81 \times 10^6 \ \mathrm{M}_\odot$ y una resolución espacial de $\epsilon = 0.7$ kpc. Esta resolución se complementa implementando modelos de procesos físicos que ocurren por debajo del límite de resolución, lo que se conocen como modelos sub-red (*subgrid models*). Estos modelos incluyen por ejemplo la formación estelar o los procesos de retroalimentación o *feedback*, y nos permiten estudiar con detalle los procesos de formación y evolución de galaxias en las inmediaciones de los cúmulos de galaxias.

Primero, se emplea un algoritmo llamado SUBFIND para identificar halos y subhalos de materia oscura, agrupando partículas en estructuras coherentes, como galaxias y cúmulos. Después, se captura la historia de fusiones jerárquicas de halos mediante un algoritmo llamado SPIDERWEB, el cual da los denominados *merger trees* de galaxias, permitiendo el seguimiento de la evolución de las galaxias a lo largo del tiempo. Estos algoritmos permiten ordenar los datos proporcionados por las simulaciones, de manera que habilitan rastrear la evolución de las galaxias a medida que se integran al cúmulo desde entornos menos densos, posibilitando identificar los mecanismos principales que conducen al cese de actividad en la formación estelar de estas galaxias.

Con esa finalidad, se selecciona una muestra de galaxias que termina cayendo dentro del radio virial (r_{200c}) del cúmulo central en cada simulación, imponiendo además un límite inferior de masa estelar de $10^8 \ \mathrm{M}_\odot$ en $z = 0$, para garantizar galaxias resueltas por al menos unas decenas de partículas de la simulación. Posteriormente, se examina la relación color-masa estelar de estas galaxias, confirmando que las galaxias rojas (con poblaciones estelares viejas y, por tanto, con formación estelar apagada) tienden a residir dentro del radio virial,

mientras que las galaxias azules (con poblaciones estelares jóvenes y, por tanto, con formación estelar activa) se encuentran principalmente en las afueras del cúmulo.

A continuación, se analizan las propiedades de las galaxias al momento de caer en el cúmulo, clasificándolas como "pre-procesadas" (ya apagadas) o "post-procesadas" (con formación estelar activa). Se encuentra que aproximadamente el 73% de las galaxias están pre-procesadas al entrar en el cúmulo, siendo estas principalmente galaxias de baja masa.

Para las galaxias pre-procesadas, se estudian dos mecanismos principales de apagado: el auto-apagado (*self-quenching*) y el procesamiento en su propio halo. El auto-apagado se analiza mediante la correlación entre la tasa de formación estelar y la tasa de acreción del agujero negro supermasivo en el centro de la galaxia en cuestión, encontrando que aproximadamente la mitad de las galaxias albergando un agujero negro supermasivo podrían haber sido apagadas por la retroalimentación del AGN (*Active Galactic Nucleus*). Las galaxias más masivas tienden a apagarse antes del último evento de acreción en modo cuásar, debido a la eficiente retroalimentación de sus agujeros negros centrales más masivos, mientras que las menos masivas a menudo muestran una decorrelación, probablemente debido a agujeros negros más pequeños incapaces de apagar la formación estelar. Por otra parte, el procesamiento en su propio halo se examina analizando la masa del halo del grupo del que provienen las galaxias antes de pertenecer al cúmulo central. Este procedimiento revela que, al menos, alrededor del 25% de las galaxias pre-procesadas provienen de grupos lo suficientemente masivos (con masas superiores a 10^{14} M$_\odot$) como para haberlas apagado *in situ*, lo que sugiere que ya han sido procesadas en estos entornos de alta densidad antes de ingresar al cúmulo central.

En cuanto a las galaxias post-procesadas, que representan alrededor del 27% de la muestra, se centra el análisis en el proceso conocido como *ram pressure stripping*, donde el componente gaseoso de las galaxias, tanto el frío como el caliente, es eliminado, debido a la presión ejercida por el movimiento relativo de las galaxias que caen al medio intracumular. Se encuentra que la gran mayoría de estas galaxias pierden su contenido de gas frío, el cual es el combustible necesario para formar estrellas, poco después de entrar en el radio virial del cúmulo, lo que eventualmente conduce al apagado de su formación estelar. Esto indica que el *ram pressure stripping* es el mecanismo principal responsable del apagado de las galaxias en entornos altamente densos. Sin embargo, también se determina que existe una pequeña fracción que podría ser apagada por fuerzas de marea producidas por el potencial gravitatorio del cúmulo central sobre las galaxias, o que ciertas galaxias consumieran su contenido de gas frío formando estrellas antes de ingresar al cúmulo por estar aisladas y no recibir inyecciones de gas frío suficientes.

En general, los resultados muestran que los cúmulos de galaxias son entornos extremadamente eficientes en extinguir la formación estelar para las galaxias que se incorporan a estos entornos. También se determina que el apagado de formación estelar se produce a través de una combinación de mecanismos físicos, incluyendo la retroalimentación o *feedback* de agujeros negros supermasivos, el procesamiento en grupos masivos previos y el *ram pressure stripping* al adentrarse en entornos densos. Estos hallazgos concuerdan con las observaciones de una mayor fracción de galaxias rojas (con poblaciones estelares envejecidas) en los entornos más densos de los cúmulos, y contribuyen a una mejor comprensión de la evolución de las galaxias en diferentes entornos cósmicos. Por consiguiente, pueden ayudar a limitar los modelos teóricos de formación de estructuras y evolución de galaxias dentro del marco cosmológico ΛCDM.

Contents

1 | Introduction

Throughout the entire human history, our fascination with the cosmos has been present; starting from the earliest civilizations gazing at the night sky, to modern-day discoveries, our desire to understand the Universe has been a driving force behind scientific research.

Among all the major pursuit in modern astrophysics, galaxy formation and evolution is considered one of the most significant research of this kind. In this topic, the impact of the environment upon the evolution of galaxies has come in front of fundamental importance to be researched. Most notably, the study of galaxy clusters, which are the largest gravitationally-bound structures in the Universe, since they give a great opportunity of researching the interconnections between the galaxies and their local surrounding.

One of the primary objectives of this research is to delve into the specific mechanisms driving the suppression of star formation, known as quenching, within galaxy clusters. While quenching can occur through various means, such as internal processes within galaxies or interactions with external factors, the main focus in this work lies on the latter. This is often referred to as environmental quenching, which is the process by which galaxies are inhibited in their ability to form stars as a consequence of their surroundings' influence in clustered regions. Galaxy clusters represent extreme environments characterized by high densities of galaxies and hot intracluster gas. These clusters can exert significant hydrodynamic, gravitational, and radiative effects on their member galaxies, leading to a quiescent galaxy population in those regions. Understanding the dominant mechanisms behind environmental quenching within clusters is crucial for deciphering how these environmental factors influence the evolution of galaxies over cosmic time.

In order to achieve this, we use the present state-of-the-art cosmological simulations to identify the processes behind quenching inside galaxy clusters, as well as in their surroundings. Through the use of these numerical simulations, we are able to investigate the manner in which gravitational forces, gas dynamics, and different types of feedback govern the outcomes of galactic systems within such gigantic cosmic structures. By analysing the enormous amount of output data produced by these simulations, we intend to pinpoint the factors responsible for the cessation of star formation activity in the cluster's surroundings, and also to identify the degree of significance of the different physical processes involved.

This work is especially relevant when considering modern astrophysics, since not only allows learning about the role of environment in galaxy evolution, which is important for improving the theoretical models of structure formation and galaxy evolution within the ΛCDM standard cosmological model. But also, environmental quenching is a major factor responsible for observed attributes of galaxies residing in clustered regions, where the morphology-density (e.g., Dressler 1980; Postman & Geller 1984; Gomez et al. 2003) and

colour-density (e.g., Hogg et al. 2003; Blanton et al. 2005; Baldry et al. 2006) relations are widely discussed. Thus, through the identification of the basic principles we will have the opportunity to better contribute and fit our theoretical knowledge with the data obtained from observations, this leading to a deeper comprehension of galaxy evolution in different cosmic conditions.

In recent years, various studies employing different methodologies have contributed to our understanding of the mechanisms driving galaxies into a quenched state. Analytic models have been instrumental (e.g., Fujita 2004; Mok et al. 2014; Contini et al. 2020), as well as semi-analytic approaches (e.g., De Lucia et al. 2012; Wetzel et al. 2013; Henriques et al. 2017; Stevens & Brown 2017; Cora et al. 2018; Contini et al. 2019). Furthermore, hydrodynamical cosmological simulations have played a crucial role (e.g., Bahé et al. 2013; Bahé & McCarthy 2015; Taylor et al. 2017; Pallero et al. 2019; Wright et al. 2019; Donnari et al. 2021) in determining the relative importance of these mechanisms. Following with these studies, our aim is to contribute to this paradigm of research by employing a set of hydrodynamical cosmological simulations.

In the following subsection, a brief general introduction about cosmological simulations is given, followed by a more specific overview of the suit of simulations used in this work in 2.1. In 2.2, the algorithm used to identify dark-matter haloes and subhaloes is described, and in 2.3 the algorithm used to retrieve the hierarchical merger histories of these subhaloes. In 2.4 and 2.5, the star formation histories and the relevant black hole physics are introduced, respectively. In 3.1 the selection of the relevant subhaloes to our objective is presented. In 3.2, we present a colour-stellar mass diagram and in 3.3 we present some properties of the subhaloes when they are accreting into clusters. In 3.4 and 3.5, we present different mechanisms responsible for the quenching separated for those subhaloes accreting the cluster already quenched and star forming, respectively. Finally, in 4, we summarize our conclusions.

Cosmological simulations

Cosmological simulations are a precious instrument in modern astrophysics. These tools have become a virtual laboratory for astrophysicists, enabling us to explore the origin and development of cosmic structures. For this reason, they are widely used for astrophysical research due to their capacity to answer many relevant questions regarding different timeframes and types of cosmic systems, which are not viable to deliver observationally, at least for now.

Fundamentally, cosmological simulations are numerical computational models that aim to reproduce the evolution of the Universe. Usually, the physics present in these simulations are derived from the ΛCDM cosmological standard model. In this model, the Universe is dominated by cold dark matter and dark energy. The first, is the key ingredient and the main driver of structure formation, whereas the latter provides the expansion of the Universe in which the studied processes occur. There are two main approaches to making cosmological simulations (Vogelsberger et al. 2020):

- **N-body simulations**: Only the gravitational interactions between individual particles representing the dark matter are simulated. To do so, they usually take a cubic spatial region with periodic boundary conditions. The initial conditions are commonly taken from the statistical spatial primordial fluctuations in the density field, which are typically measured observationally in the cosmic microwave background. Then, the known

physics are applied to evolve time all the way to the present, revealing the formation of large-scale structure of the universe, including the formation of cosmic filaments, voids, and the clustering of dark matter haloes.

- **Hydrodynamic simulations**: In addition to dark matter, hydrodynamic simulations also model the behavior of baryonic matter in the universe. This baryonic matter consists only of a small part of the cosmic composition. However, at the same time it constitutes the best source of observations, as well as the most expensive part of the simulations from a computational point of view, given that these particles interact hydrodynamically. In consequence, the types of interactions to be taken into account are multiplied, as well as the particle types, such as gas particles, star particles, and black hole particles.

  The huge spatial and temporal dynamical ranges in these simulations come with a high computational cost, and as a consequence, a compromise between resolution and spatial coverage has to be found in order to execute these codes in a reasonable timeframe. For the time being, it is impossible to reach the resolution to reproduce the galaxy formation models in cosmologically scaled simulations. Thus, these interactions are modelled using subgrid models. These models are used to model all the physical processes that operate below the resolution limit of the simulations and have to be carefully calibrated in order to generate scientifically accurate data. For example, galaxy formation models have to be added in this way, including various physical phenomena such as gas cooling/heating, star formation, injections of energy and angular momentum due to supermassive black holes and massive stars, supernovae and active galactic nuclei feedbacks, etc.

  With all this, the code runs through the numerical solution of the coupled equations of gravity, fluid dynamics, and radiative transfer with the cosmic framework stipulated, which track the development of matter density distribution from the smooth and nearly uniform early Universe to the complex structure of the present Universe, being able to give detailed insights into galaxy formation and the properties of the intergalactic medium.

The results obtained from cosmological simulations are usually subjected to verification and validation processes, and they become accepted when the output of the simulations are statistically consistent with some observable constraints, such as halo mass functions or galaxy luminosity functions. To check that the simulated data are in accordance with these observables, the observational data is usually gathered from large surveys, such as the Sloan Digital Sky Survey (SDSS) (Eisenstein et al. 2011).

With increasing speed in computational capabilities, these simulations are predicted to be more and more precise in the future, covering larger spatial regions and higher resolutions. This will provide more opportunities to study areas below the current resolution limits without having the need of implementing and calibrating subgrid models, and this way, to discover new science.

2 | Simulations and Methodology

In this chapter, we will be having a deeper look at the methodological background of this study. We introduce the employed simulations, as well as indicating the procedures employed to identify the galaxies, to track them down through the time, and also we will give some definitions and references to be able to follow the results satisfactorily.

2.1 C-EAGLE simulations

The Cluster-EAGLE (C-EAGLE) simulation project (Barnes et al. 2017) is a set of cosmological hydrodynamical zoom-in simulations (Tormen et al. 1997) of 30 massive galaxy clusters in the mass range of $(10^{14} < M_{200c}/M_\odot < 10^{15.4})$ [1] . The employed cosmological model is the standard ΛCDM with parameters from (Planck Collaboration et al. 2014): $\Omega_b = 0.04825$, $\Omega_m = 0.307$, $\Omega_\Lambda = 0.693$, $h \equiv H_0/(100\text{km}/(\text{s} \times \text{Mpc})) = 0.6777$.

This simulation project was motivated by the limitations of existing cluster and galaxy simulations, such as the EAGLE project (Schaye et al. 2015; Crain et al. 2015; McAlpine et al. 2016; EAGLE-Team 2017) (Evolution and Assembly of GaLaxies and their Environments). The main limitation of these simulations is that due to the required resolution and the complex nature of the subgrid models involved, they require a huge computational cost, constraining their applicability to periodic cubes measuring approximately 100 Mpc or smaller. While such a volume may encompass numerous galaxy groups (with mass ranging from 10^{13} to 10^{14} $M_\odot$), it is exceedingly rare to encounter big galaxy clusters (with mass around 10^{15} $M_\odot$) within this limited volume. Consequently, evaluating the capability of these calibrated models to accurately replicate structures like galaxy clusters becomes challenging due to the scarce population of these big clusters, and as a consequence, having a low statistical sample. Also, testing their ability to capture galaxy formation across various environments proves to be equally challenging.

However, until simulations at the resolution of EAGLE, but with orders of magnitude larger volume, become computationally feasible, progress can still be made through zoom-in simulations (Tormen et al. 1997), where only a selected small part of the universe is simulated at high resolution. Like this, zoom-in simulations are able to simulate environments that can not be present in the volumes feasible with their highest resolution.

For creating these zoom-in simulations, first a large N-body box run is performed, which will be the parent simulation. Then, a targeted approach is employed, where only a small

---

[1] M_{200c} denotes the total mass within a sphere of radius r_{200c} centred on the potential minimum of the cluster, within which the average density is 200 times the critical density of the Universe.

segment within the parent simulation is modelled in high resolution, including baryons and their hydrodynamical interactions, as well as subgrid physics models. This resimulated region is centred on a region of interest, which in our case is a galaxy cluster. The majority of the space is filled with low-resolution boundary particles, which interact only through gravitational forces. In this manner, appropriate tidal fields and large-scale modes are generated within the high-resolution region.

The parent simulation is sourced from the project MACSIS (MAssive ClusterS and Intercluster Structures) (Barnes et al. 2016), which encompasses a cubic periodic volume of (3.2 Gpc)^3, sufficiently large to encompass a sample of the most massive haloes predicted in the ΛCDM cosmology. Subsequently, 30 haloes uniformly distributed in the mass range are chosen, with the condition of not having a more massive neighbour halo within $20 \times r_{200c}$. From this selection, the haloes are subjected to resimulation using the hydrodynamical EAGLE code. This code is a significantly altered version of the N-body Tree-PM smoothed particle hydrodynamics (SPH) code P-GADGET-3, as detailed in Springel (2005). The C-EAGLE runs adopt the same mass resolution ($m_{\text{gas}} = 1.81 \times 10^6 \text{M}_\odot$) and physical spatial resolution ($\epsilon = 0.7$ kpc) as the largest periodic volume of the EAGLE suite (Ref-L100N1504). However, a slight modification has been made in the subgrid physics, having an enhanced AGN feedback, with the so-called Ref-AGNdT9 model.
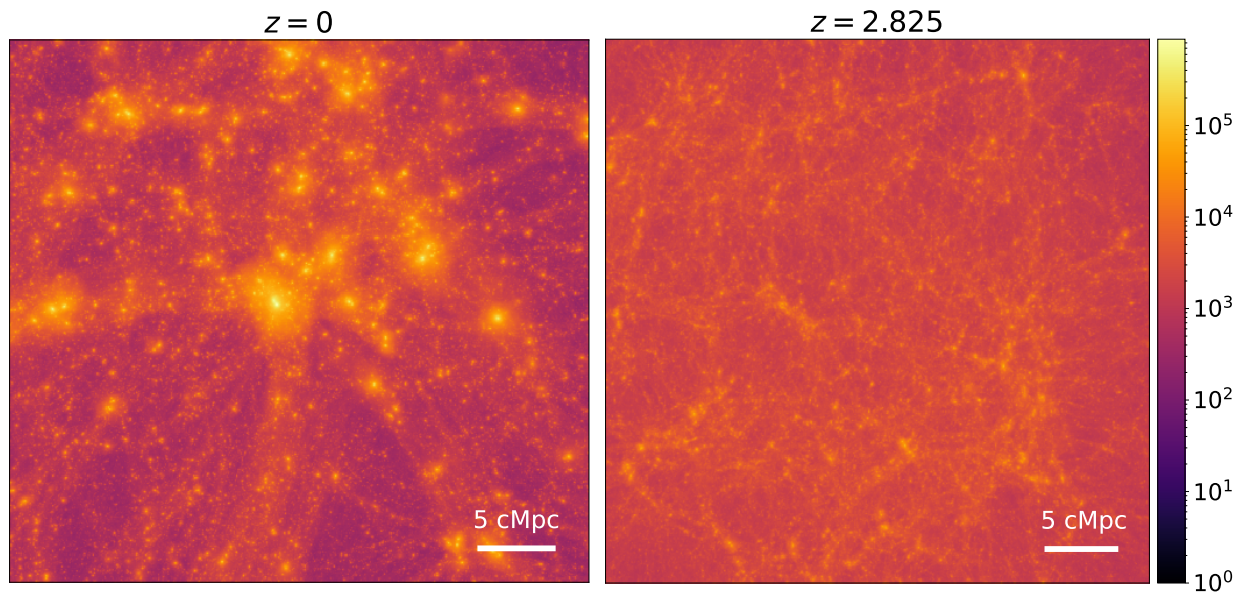

Figure 2.1: Spatial distribution of dark matter for run CE-21. The images are a projection of all the dark matter particles along the simulation z axis, centred in a 40×40 comoving Mpc square. In the left panel, the distribution for $z = 0$ (present) is represented, and in the right, the one for $z = 2.825$ (11.52 Gyrs ago). The colormap represents the number of dark-matter particles per bin. The white line in the bottom right corner of each panel indicates the comoving spatial scale.

The C-EAGLE simulations incorporate the *Hydrangea* sample (Bahé et al. 2017), which was designed to study the evolution of galaxies as their environment transitions from an isolated field to a dense cluster. This sample extends the zoom region to ten virial radii for 24 of the 30 C-EAGLE clusters, while the other six runs were simulated with a zoom region only for $5 \times r_{200c}$. As a consequence, the *Hydrangea* simulations are an ideal laboratory to characterize the effects of the high-density environments on individual galaxies, enabling us to pinpoint the impact of the environment on quenching the star formation of galaxies as they enter the cluster. Detailed information for each simulation is provided in Table 2.1, displaying the scale of the central clusters in each run with both radius (r_{200c}) and mass (M_{200c}), covering from smaller clusters such as run CE-0 to the largest, in CE-29. This table also includes additional characteristics, such as the count of galaxies and their positions within the parent simulation.

The main output of the simulations consists of 30 snapshots between $z = 14$ and $z = 0$, 28 of which are equally spaced in time ($\Delta t = 500$Myr) with two additional snapshots at $z = 0.366$ and $z = 0.101$ for each run. These two additional snapshots are included to facilitate comparisons with the output of EAGLE simulations.

In Figure 2.1, a plot showing the spatial distribution of the dark matter particles for run CE-21 is shown for different stages of the simulation, the present time, $z = 0$, and $z = 2.825$. These figures depict the progression of structure formation, illustrating the transformation of a neatly uniform matter distribution into galaxy clusters through gravitational attraction.

In the following pages, we will be tracking the galaxies that form the galaxy clusters such as the one that can be seen at the left panel of Figure 2.1, and will see how the progressive change in their surroundings affects their properties.

Magnitude calculation

One of the main outputs of these types of numerical simulations is the stellar mass of galaxies, and the same happens in our particular case with the C-EAGLE simulations. However, the main observable is stellar light. For this reason, the output of the simulation has to be post-processed in order to compare with observable galaxy luminosity functions. This is exactly what is done in Negri et al. (2022), and we will use the results produced in this paper in our work.

In the mentioned work, each stellar particle gets treated as a single stellar population (SSP), which is characterized by its initial mass, metallicity, and age. Then, the fully empirical E-MILES state-of-art stellar population model (Vazdekis et al. 2016), the Padova isochrones (Girardi et al. 2000), and the Chabrier (2003) initial mass function (IMF) are used to calculate the full spectral energy distribution (SED) of each stellar particle. After that, all the SEDs are summed within a selected spherical aperture, as well as convolved with the response curves of selected filters from various photometric systems. This way, galaxy broadband luminosities are obtained. This process is done for all output redshifts and for every galaxy with a total stellar mass greater than $10^{7.5}M_\odot$, corresponding to a few tens of star particles. Finally, dust attenuation due to the interstellar medium (ISM) is applied to the integrated spectra, following the model presented in Trayford et al. (2015), but with a slight modification as detailed in Negri et al. (2022).

Halo ID	r_{200c} [pMpc]	M_{200c} [$\log(\mathrm{M}/\mathrm{M}_\odot)$]	x [pMpc]	y [pMpc]	z [pMpc]	$N_{galaxies}$ $< r_{200c}$	$N_{galaxies}$ $< 10r_{200c}$
CE-0	1.03	14.07	313.65	2218.64	2652.71	36	181
CE-1	1.02	14.05	2598.97	2552.80	2266.29	34	163
CE-2	1.02	14.05	2889.69	2880.09	355.44	34	163
CE-3	1.09	14.14	2608.58	2831.41	908.38	49	243
CE-4	1.17	14.23	1720.84	2253.49	2670.52	68	322
CE-5	1.09	14.15	583.22	908.50	1669.79	42	294
CE-6	1.27	14.34	2624.03	2241.14	304.69	76	380
CE-7	1.27	14.34	1272.32	2452.95	1288.05	76	452
CE-8	1.23	14.30	486.08	735.81	357.66	67	338
CE-9	1.39	14.46	1368.63	1452.69	2207.20	84	486
CE-10	1.29	14.36	2616.89	1602.52	1876.43	90	446
CE-11	1.43	14.49	2564.49	678.34	1356.74	109	537
CE-12	1.55	14.60	1165.85	1386.20	1010.20	148	506
CE-13	1.57	14.61	998.80	1511.46	1963.65	131	498
CE-14	1.62	14.66	276.94	1459.94	2042.48	179	734
CE-15	1.71	14.73	2015.45	737.45	1738.86	203	957
CE-16	1.74	14.75	717.52	2244.68	609.33	202	1179
CE-18	1.87	14.84	793.71	864.02	1612.59	261	1061
CE-21	1.99	14.93	1139.47	909.91	948.80	306	1901
CE-22	2.14	15.02	2078.36	2319.21	843.85	362	3153
CE-24	2.27	15.09	306.88	996.23	2870.46	425	1701
CE-25	2.36	15.15	1028.05	1272.37	1276.27	497	2185
CE-28	2.50	15.22	1390.16	1049.82	2040.15	556	2804
CE-29	2.82	15.38	1070.13	2140.38	1498.16	826	3788

Table 2.1: Overview of the 26 C-EAGLE simulations from the *Hydrangea* sample at redshift $z = 0$. The radii within the average density equals 200 times the critical density; the total mass enclosed in these radii; the positions of the potential minimums of the clusters in the $(3.2 \text{ Gpc})^3$ parent simulation; and the number of galaxies with $M^{\mathrm{star}}_{30\mathrm{pkpc}} > 10^9 \mathrm{M}_\odot$ within 1 and 10 r_{200c} from the potential minimum of the cluster are provided. (Bahé et al. 2017).

2.2 Halo & subhalo identification

Halo & subhalo identifiers play a crucial role in cosmological simulations by providing a means to group individual simulation particles into coherent structures, such as galaxies and galaxy clusters. Without these identifiers, we would solely rely on particle data, making it impossible to discern meaningful structures and their evolution within the simulated universe. Since we intend to investigate the effects that galaxies suffer from their environment, it is essential for us to use a subhalo finder, which in our case will be SUBFIND (Springel et al. 2001).

The SUBFIND algorithm is a widely used method to identify and characterize the substructures within dark matter clumps formed in cosmological simulations. This algorithm not only defines subhaloes as locally overdense regions, but also self-bound particle groups within a larger parent group. In this way, it can detect hierarchies of the substructure. The parent group will consist of a particle ensemble preselected using a standard Friends-Of-Friends (FOF) linking length. The FOF algorithm is one of the earliest and simplest halo finding algorithms, which consists of considering dark matter particles to belong to the same halo if they are within a certain linking length to each other. In this case, a linking length of $b = 0.2$ times the mean interparticle distance is applied. This means that if particle A is linked to particle B, and particle B is linked to particle C, then particles A, B, and C are all part of the same group.

However, this simple algorithm can lead to haloes of irregular shape and sometimes linking together two separate structures, on the contrary, SUBFIND can deal with those problems. First, SUBFIND detects locally overdense regions by gradually reducing a global density threshold until distinct regions merge to create a unified domain. Once we have some subhalo candidates, an unbinding procedure is executed to see that all the dark matter particles linked are self-bounded. This is achieved by first computing a velocity centre, which represents the average velocity of particles within the group. Then, individual particle velocities are determined relative to this centre. This process allows for the identification of particles with kinetic energy that exceeds the gravitational potential energy, indicating that they are unbound and thus not included in the halo. An example result can be seen in Figure 2.2. Originally, this algorithm was developed for dark-matter only simulations. Nevertheless, in Dolag et al. (2009) this algorithm is suitably modified to account for the presence of gas and star particles present in hydrodynamical simulations, since the density contribution from the gas component is slightly smoother than that from the dark matter component (thanks to the gas pressure), whereas star particles generally trace a highly concentrated density field, resulting in a more noisy total density field compared to pure dark matter runs.

More algorithms are available for the same purpose, and a comparison between several of them is developed in Onions et al. (2012). For example, six-dimensional phase-space based subhalo finders are studied, like ROCKSTAR (Behroozi et al. 2012), which, in theory, should do better in very dense regions. However, this study finds a remarkable agreement between the halo finders that are based on widely different algorithms and concepts. Hence, it is concluded that none of the phase-space based finders present a significant improvement upon the best of the more traditional real-space based finders as SUBFIND, at least for now. For this reason, we decide to use this more simple and efficient algorithm in order to identify subhaloes.
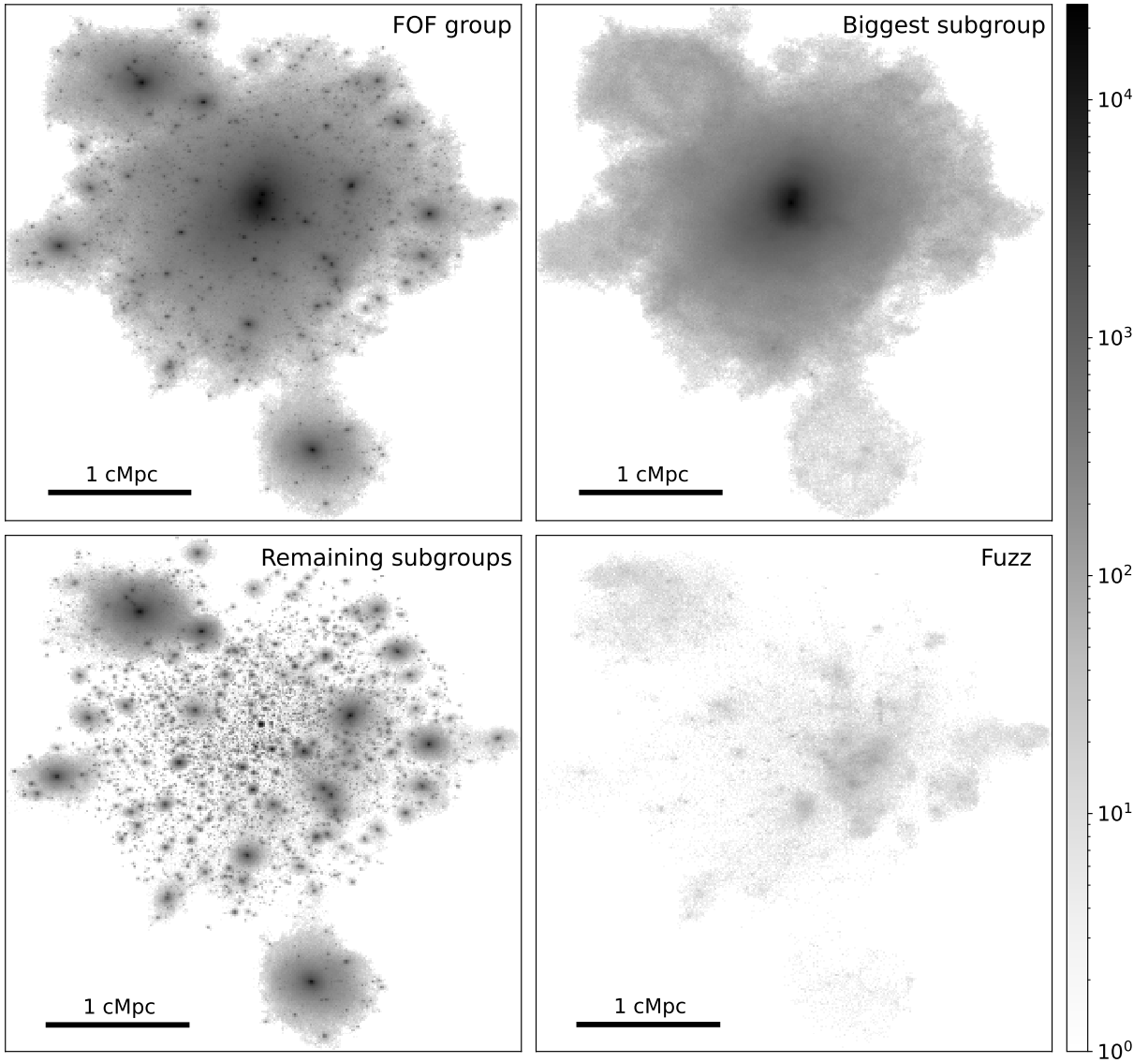
Figure 2.2: Example for a subhalo identification with SUBFIND. The shown group is the central group of run CE-0 at $z = 0$. The top left panel displays the whole FOF group. The largest subhalo, constituting the background halo, is shown in the top right panel, while the remaining subhaloes can be seen collectively in the lower left panel. Particles not gravitationally bound to any subhalo form the "fuzz", as illustrated in the lower right panel. The colormap is logarithmically scaled and represents the number of dark-matter particles in each pixel.

2.3   The galaxy merger tree

SUBFIND identifies structures at a single point in time, or what is the same, at a single snapshot. However, following the galaxies in their evolution over multiple snapshots is of great importance when analysing a simulation. Therefore, an additional procedure is required, that is to create galaxy merger trees. A merger tree is a representation of the hierarchical merging
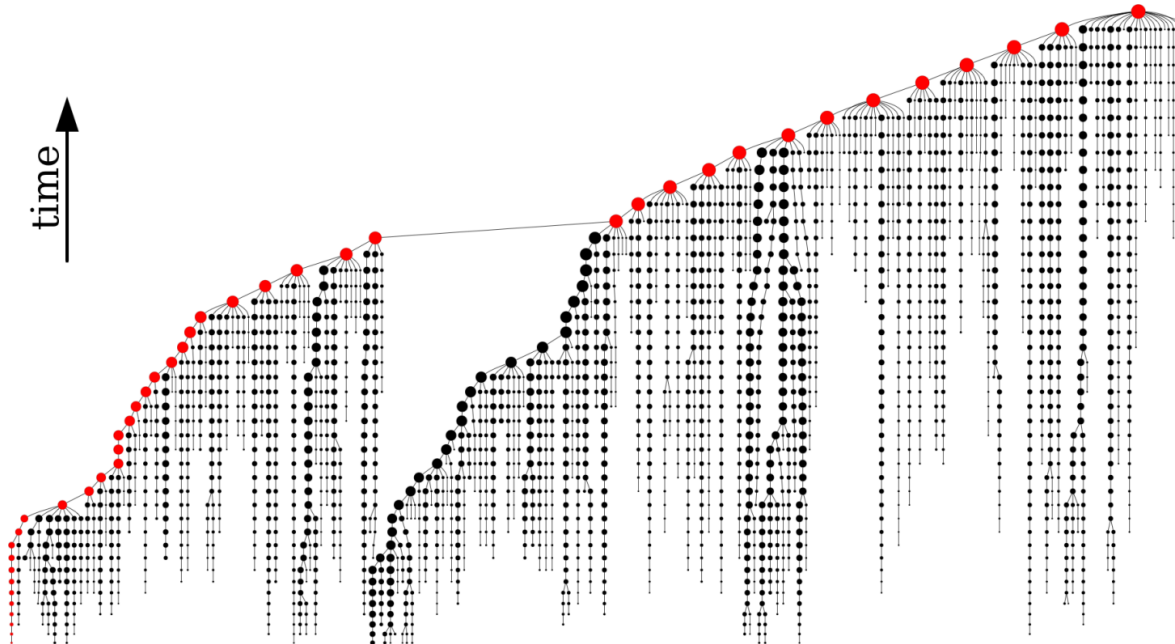
Figure 2.3: A graphical representation of a merger tree. Each circle corresponds to a halo, with lines extending upwards to its descendants and downwards to its ancestors. The size of each circle is proportional to the halo's mass, and red circles indicate the main progenitor. (Smith & Lang 2019).

history of haloes in a cosmological simulation. When it is executed at a certain cosmic time or snapshot, it captures the complete merger history of the subhaloes up to that point. Generally, the output provides unique IDs of the subhaloes in that snapshot, plus a fixed ID for $z = 0$ that identifies them univocally, enabling us to trace them across snapshots, or, what is the same, to track them down in time.

Consequently, the merger tree provides a means to identify the progenitors (ancestors) and descendants (successors) of galaxies, facilitating us to track the transformation of galaxies as they transition from being isolated or in smaller groups to becoming part of the larger cluster environment. For this reason, employing a merger tree in our work enables us to track the star formation quenching process of the galaxies as they fall into a cluster.

In this context, the main progenitor is defined as the primary ancestor of a given halo at each snapshot in time, these being the haloes containing the most bound particles, that are usually the most massive. It represents the dominant evolutionary pathway of the halo, tracing its most significant merging and accretion events. Therefore, by tracking only the main progenitor, we are able to capture the dominant evolutionary processes that have shaped the properties of the final descendants, including the star formation. This way, the complexity and computational cost associated with tracking multiple merging branches is greatly reduced. In Figure 2.3, an example of the history of merging branches is represented, showing the main progenitor at each cosmic time in red.

The trees examined in this study were generated using the SPIDERWEB algorithm (see Bahé et al. 2019, Appendix A). In contrast to other merger tree algorithms (e.g., Rodriguez-Gomez et al. 2015; Qu et al. 2017), SPIDERWEB was specifically developed to trace descen-

dants effectively in dense surroundings, considering more than one possible descendant for each subhalo. It defines descendants as all subhaloes that have particles in common between successive snapshots, and then prioritizes them to select the most relevant descendant. This approach is particularly significant in galaxy groups and clusters, where interactions between galaxies are frequent.

2.4 Star formation histories

The star formation history (SFH) of a galaxy, as its name reveals, is essentially a chronicle of how stars form in the galaxy throughout its existence in time. We can imagine it graphically like the star formation rate (SFR), which is just the mass of the formed stars per unit time, plotted against cosmic time. This tool can reveal when a galaxy had its peak star formation, and even when it got quenched, if that is the case. Consequently, it is quite useful for us to infer the conditions and environments that influenced star formation activity. For example, a galaxy with a relatively constant star formation rate may indicate a stable environment, whereas a galaxy experiencing sporadic bursts or declines in star formation may suggest interactions with different feedback mechanisms or mergers with other galaxies.
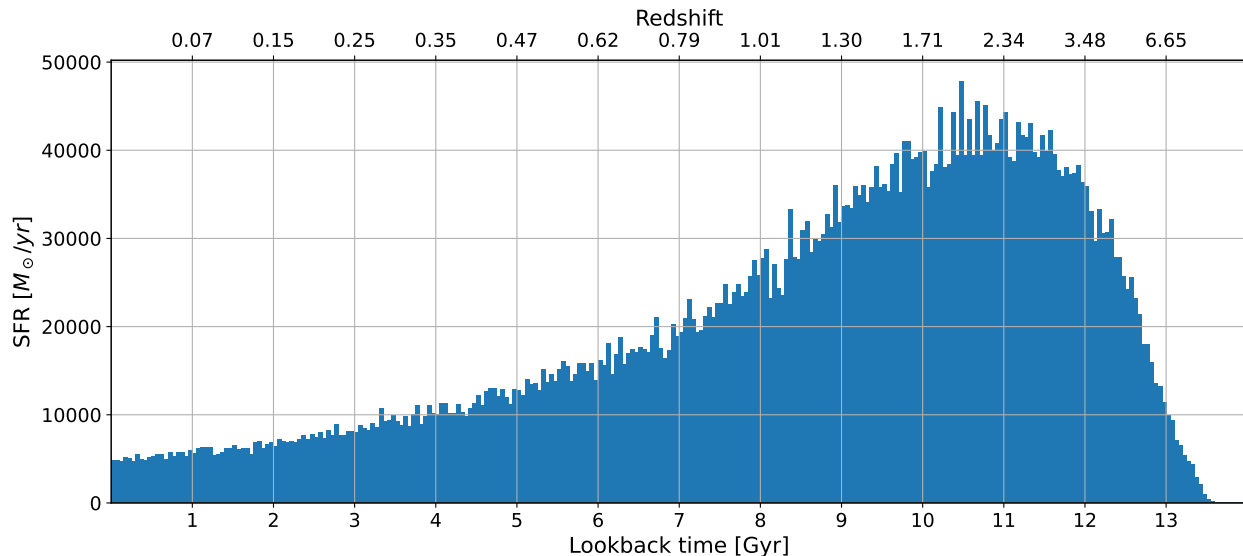

Figure 2.4: Star formation history for all the subhaloes in run CE-29. The star formation rates for each subhalo are added to form the total star formation rate. The time axis is represented in redshift (top) and lookback time (bottom), meaning that the present time is on the left side of the plot.

However, the snapshots mentioned above and the group files produced by SUBFIND, only provide SFR data approximately every $\Delta t = 500 \text{Myr}$. To enhance this time resolution, complementary information provided in the output can be used in addition to snapshots. These files, contain the information of when simulation cold gas particles are converted into star particles. Hence, to create SFHs with high time resolution, one can proceed by taking all the stellar particles of a subhalo and doing a histogram of their creation time weighted

with their initial mass. This way, we obtain time bins containing the stellar mass created in that lapse of time, which will be useful for the future analysis. An example SFH for all subhaloes in the run CE-29 is plotted in Figure 2.4, when the peak of SFR can be found at around 10.5 Gyrs of lookback time, which corresponds approximately to $z = 2$, a period known as the Cosmic Noon of galaxy formation.

2.5 Black hole physics

Black holes are objects characterized by regions of spacetime where gravitational forces are so intense that they prevent anything, including light, from escaping. The boundary for this to happen is known as the event horizon and in the centre of this horizon lies a singularity, a point of infinite density and curvature, where the laws of physics as we currently understand them break down. When matter with a significant angular momentum falls into a black hole, it can form an accretion disk, a rotating disk of gas and dust spiralling inward due to the black hole's gravitational attraction. These particles get accelerated as they lose gravitational potential energy, also releasing energy in the form of intense radiation and jets of particles. This radiation can disrupt nearby gas clouds, influencing star formation by heating up to ionizing them, or even producing galactic outflows.

Usually, each subhalo will have at least one massive black hole near its centre, which will grow in mass over time as they accrete surrounding matter, in tandem with the growth of the subhalo itself. As subhaloes merge and evolve, their central black holes can also merge with others and grow by accreting gas, forming even larger black holes at the centres of massive galaxies (see Figure 2.5 for $M_\star - M_{\mathrm{BH}}$ relation), which we call supermassive black holes (SMBH). When their activity is particularly intense, these objects can impact significantly on the star formation activity of galaxies by heating or expelling gas from the galaxy (Sijacki et al. 2007). In those cases, the host galaxy is classified as hosting an active galactic nucleus (AGN).

Nevertheless, since the data stored in snapshots are insufficient to track black hole accretion and the effects produced by the AGNs, we need a finer temporal sampling. For this reason, separate files containing detailed information on when gas particles are accreted onto the BHs are produced by the code. These files contain information on every black hole in the simulations; however, a selection of supermassive black holes has been used, since these are the ones that can perform significant feedback. This selection takes into account only the most massive SMBH in a subhalo, which is almost always the central one, so it greatly reduces the amount of data.

Since we are interested in how black holes affect star formation, the parameter that correlates with this in the case of the AGNs is the black hole gas accretion rate. This physical process is detailed below the resolution limit of the simulation. As a consequence, the subgrid physics must be calibrated accurately (see Schaye et al. 2015 and Crain et al. 2015 for details). In these works, the gas accretion rate, $\dot{m}_{\mathrm{accr}}$, is specified as the minimum of the Eddington rate, which is the theoretical maximum rate at which mass can accrete onto the object without radiation pressure overcoming gravitational infall,

$$\dot{m}_{\mathrm{Edd}} = \frac{4\pi G m_{\mathrm{BH}} m_{\mathrm{p}}}{\epsilon_{\mathrm{r}} \sigma_{\mathrm{T}} c}, \tag{2.1}$$
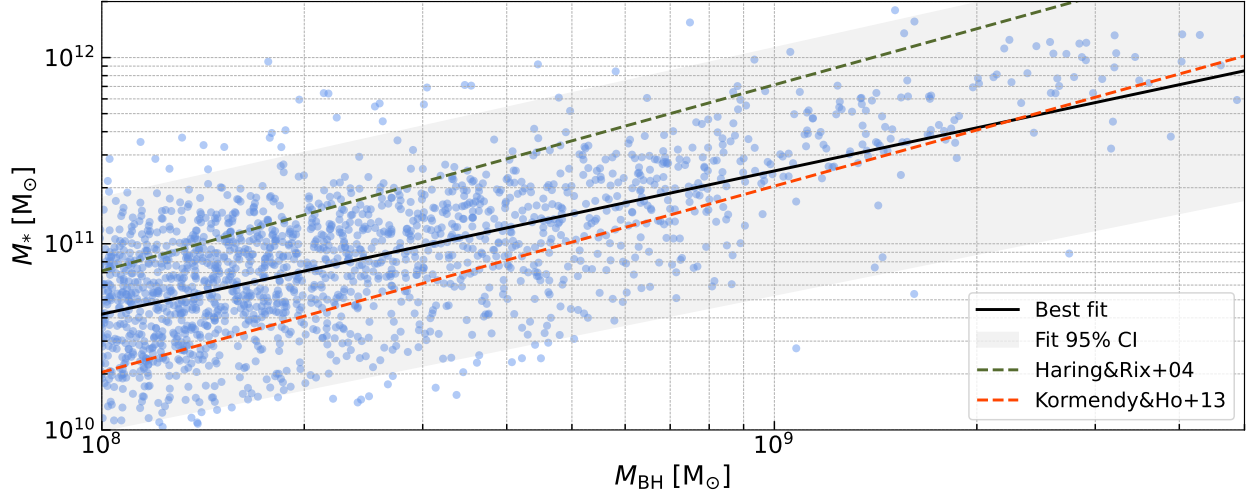
Figure 2.5: $M_\star - M_{\mathrm{BH}}$ relation for all the subhaloes with $M_{\mathrm{BH}} > 10^8 \mathrm{M}_\odot$ (to avoid contamination due to the resolution) in the Hydrangea sample at $z = 0$. A linear fit has been done for the data points (black line), representing the 95% confidence interval with the gray area. Observational relations from Häring & Rix (2004) ($M_{\mathrm{BH}}/\mathrm{M}_* = 0.0014$) and Kormendy & Ho (2013) ($M_{\mathrm{BH}}/\mathrm{M}_* = 0.0049$; canonical) are shown with green and red dashed lines, respectively.

and the simulation output, which models the Bondi & Hoyle (1944) rate applicable to spherically symmetric accretion,

$$\dot{m}_{\mathrm{accr}}^{\mathrm{out}} \propto \dot{m}_{\mathrm{Bondi}} = \frac{4\pi G^2 m_{\mathrm{BH}^2} \rho}{(c_s^2 + v^2)^{3/2}}. \tag{2.2}$$

That is, the accretion rate is given by:

$$\dot{m}_{\mathrm{accr}} = \min(\dot{m}_{\mathrm{accr}}^{\mathrm{out}}, \dot{m}_{\mathrm{Edd}}). \tag{2.3}$$

Here G is the universal gravitation constant, m_{BH} is the black hole mass, m_{p} is the proton mass, ϵ_{r} the radiative efficiency of the accretion disc, σ_{T} the Thomson cross-section, c the speed of light, c_s the speed of sound, v the relative velocity of the BH and the gas, and ρ the density of the surrounding medium.

Furthermore, the Eddington ratio (λ) is defined as the black hole accretion rate normalized with the Eddington accretion rate.

$$\lambda \equiv \frac{\dot{m}_{\mathrm{accr}}}{\dot{m}_{\mathrm{Edd}}}. \tag{2.4}$$

In this way, not only we obtain a dimensionless quantity that simplifies the comparisons across different black hole masses and environments, but also, we emphasize the upper physical limit of the Eddington accretion rate being equal to unity. As a consequence, this Eddington ratio provides insight into the efficiency of black hole accretion relative to its maximum possible rate, which is specially useful for our purpose.

Various models often categorize black hole feedback into two distinct modes: 'quasar-mode' and 'radio-mode' (see, for instance, Bower et al. 2006; Croton et al. 2006; Sijacki et al. 2007). The quasar-mode feedback predominates when the black hole accretes matter efficiently. In contrast, the radio mode becomes prominent when the accretion rate is relatively
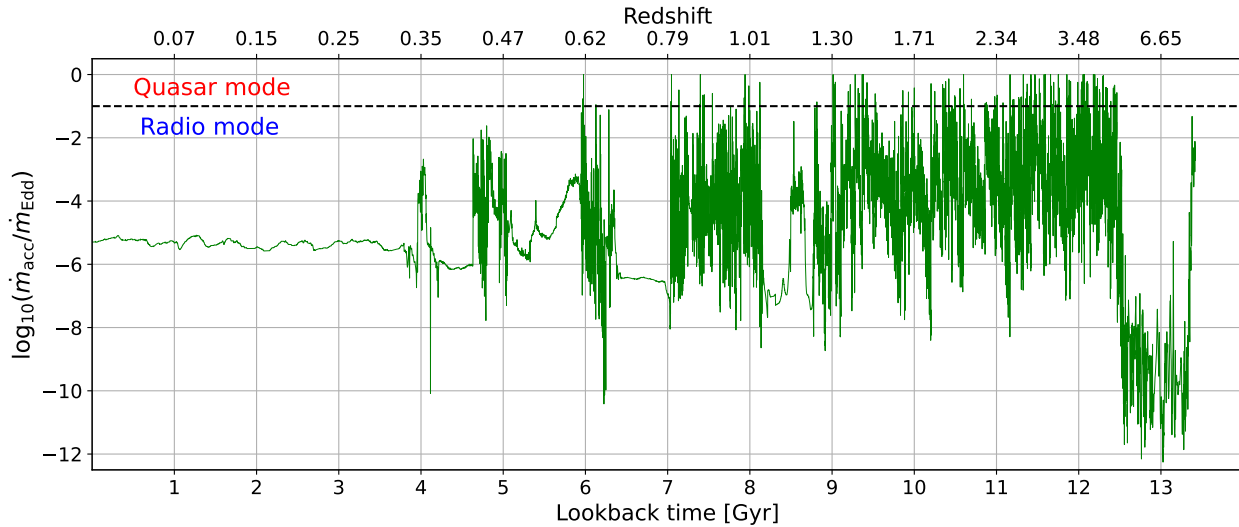
Figure 2.6: The Eddington ratio (defined in Equation 2.4) vs. time, representing the BH accretion history for the SMBH corresponding to the main halo (ID=0) for run CE-29 as an example. The horizontal dashed line indicates the $\lambda = 0.1$ threshold adopted to distinguish between quasar and radio accretion modes. The time axis is represented in redshift (top) and lookback time (bottom), meaning that the present time is on the left side of the plot.

low compared to the Eddington rate. Of course, the feedback provided by the quasar-mode will be much more efficient in star-formation quenching, and hence we will centre our analysis in this feedback mode. To differentiate between the two accreting modes, a threshold value of $\lambda = 0.1$ has been adopted for the Eddington ratio. This way, those moments at which a black hole is accreting with $\lambda > 0.1$ are considered as quasar-mode feedback, while the ones with $\lambda < 0.1$ are classified as radio-mode feedback.

An example black hole accretion rate evolution is plotted in Figure 2.6, where the SMBH corresponding to the main halo at run CE-29 has been selected to do so. In this example, it can be observed that in the last 4 Gyrs the SMBH has undergone a nearly constant low-accretion episode, while between 6 and 12.5 Gyrs has undergone a very high activity with a substantial number of quasar-mode accretion events.

3 | Results

3.1 Sample selection

The number of main progenitors in each run of the *Hydrangea* sample is very large. Nevertheless, we are only interested in some of them, given that not every main progenitor will fall into the cluster, and therefore they will not experience the effects of the dense environment.
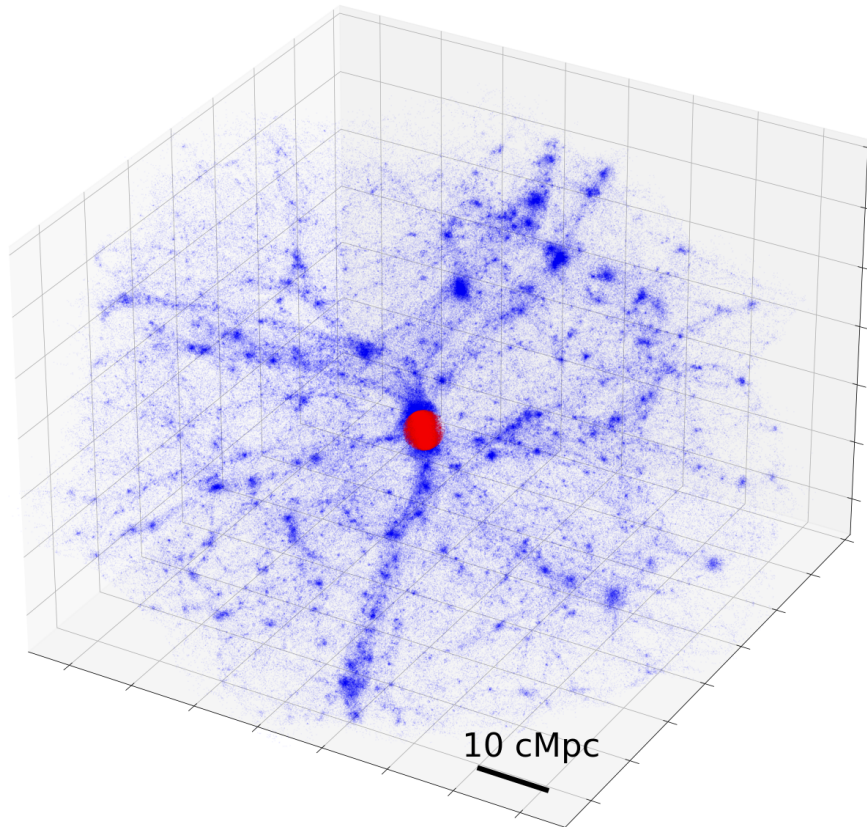

Figure 3.1: Subhalo centre positions from run CE-29 at $z = 0$. In the blue, all the subhalo centres found by SUBFIND are represented (1198166), while in red just the ones that are inside r_{200c} of the central cluster (55824).

Hence, we select a sample of main progenitor subhaloes that are inside the central cluster at $z = 0$. The central cluster or main halo is defined as the most massive halo at $z = 0$ for each run, around whom the high-resolution region is defined. A subhalo is considered to be inside the main halo if the distance to the centre of the main halo, r, is smaller than r_{200c}. In other words, a subhalo will be inside the central cluster if it is approximately inside its virial region. As a consequence, the condition that the subhaloes must fulfil to be selected is that they must be inside the central cluster at $z = 0$. This way, we make sure that the subhaloes we will analyse have undergone environmental effects provided by the central massive cluster.

In Figure 3.1, the selection made is represented graphically for the largest cluster, CE-29. Moreover, with this selection we indirectly exclude all main progenitor galaxies that lie close to the edge of the high-resolution region at some point, and therefore may be subjected to numerical artefacts, such as contamination from low-resolution particles.

In addition to the above, we impose a lower limit for stellar mass at $z = 0$, leaving out of the selection those main progenitor subhaloes with a stellar mass below $10^8 M_\odot$. With this second selection, we ensure that the selected subhaloes are resolved by more than a few tens of stellar particles, resulting in a total sample of 12351 main progenitor galaxies, which is approximately the 22% of the main progenitor subhaloes inside r_{200c} at $z = 0$, taking into account the virial radius of every main halo in each of the *Hydrangea* runs.

3.2 Colour-stellar mass relation

The consequences of the environmental quenching can be detected observationally via the galaxies' photometric properties. Since the dense environment hampers the star formation, the densest regions tend to have older stellar populations, and as a result, emit redder light.

To visualize this relation with our simulations, we used the magnitudes computed in Negri et al. (2022) to create Figure 3.2, where a rest-frame colour-stellar mass diagram is shown for the stacked 26 *Hydrangea* simulations at $z = 0$. In this figure, we separate the subhaloes inside and outside the virial region of the central cluster to be able to notice the effects of the environment on their colours. A distinct diagonal line is appreciated, namely the red sequence. It spans nearly the full range of galaxy masses for both the inside and outside populations. In addition, only for the outside population, a blue cloud can be seen, which extends to bluer colours beyond the red sequence. As expected, when we focus solely on galaxies within the cluster's virial radius, we observe a notable decrease in the population of the blue cloud, aligning with the prevalence of quenched galaxies in these inner regions. Nevertheless, a considerable number of bluish, star-forming galaxies with $M_\star > 10^9 M_\odot$ are present in the virial regions that should not be there following current observational constraints. This is thought to be a consequence of a not sufficiently effective AGN feedback for high-mass galaxies in the EAGLE code.
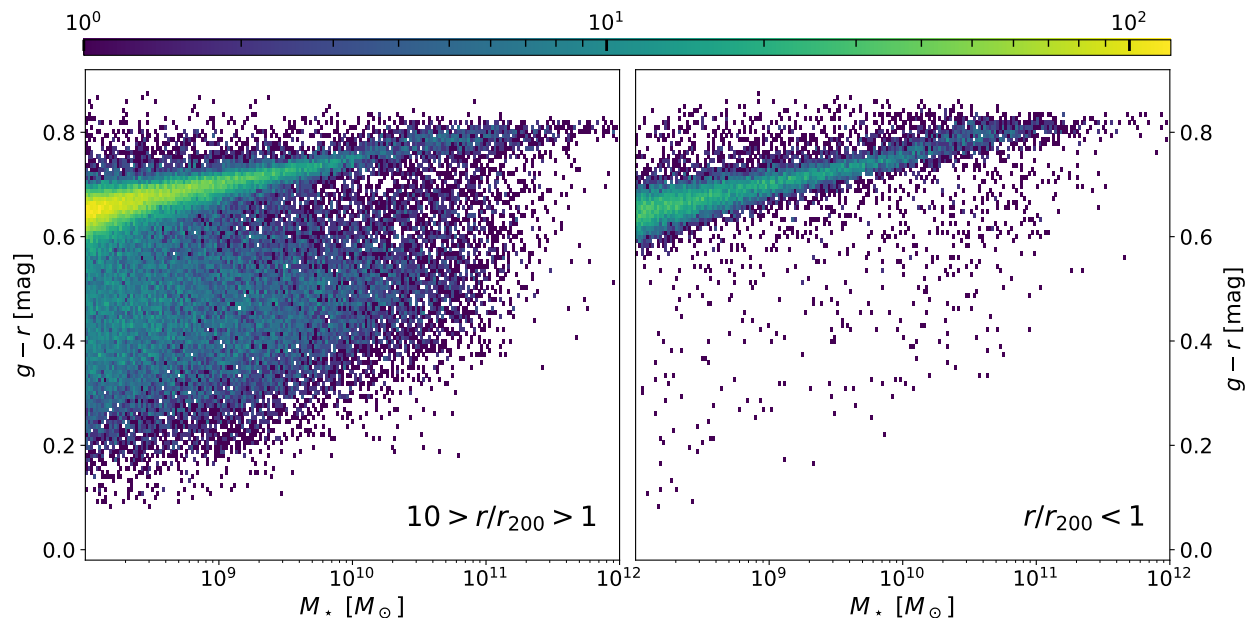
Figure 3.2: Colour-stellar mass diagram for the stacked 26 *Hydrangea* simulations at $z = 0$. The magnitudes g and r are computed inside an aperture of 30 kpc. The left panel shows all galaxies inside the high-resolution region but outside the virial region, $10 > r/r_{200} > 1$, and the right panel shows only the ones inside virial region of the central cluster, $r/r_{200} < 1$. The colour bar represents the galaxy number density in each pixel. The represented magnitudes are from Negri et al. (2022).

This leads to a well-known significant conclusion: red galaxies tend to reside both within the virial radius of clusters, where effective environmental quenching processes are prominent, and beyond, where less effective quenching mechanisms occur. Conversely, the blue galaxies almost exclusively lie in the outskirts of the cluster, where stars can keep forming and rejuvenating the stellar population without the environmental quenching processes being present. This comes in agreement with the high fractions of quenched galaxies found in the C-EAGLE cluster regions by Bahé et al. (2017). In fact, this has been known for decades, thanks to previous research based on observational surveys with the same conclusion (e.g., Gomez et al. 2003; Kauffmann et al. 2004; Poggianti et al. 2006; Moran et al. 2007; Blanton & Moustakas 2009). In the following sections, we will explore the underlying causes of this behaviour.

3.3 Population of subhaloes accreting into the main halo

The properties of galaxies accreting onto clusters can provide clues about the influence of the cluster environment, providing a starting point to understand these effects. Hence, we explore different relevant properties like the specific star formation rate or the stellar mass distributions of the galaxies when they accrete the main halo, that is, at their entry snapshot[1].

---

[1]We define as entry snapshot the first snapshot in which the target subhalo is already inside the sphere of radius r_{200c} centred on the main halo centre.

To do so, we categorize the entry status of a galaxy based on its level of star-formation activity at that time, classifying it as either star-forming or quenched.

Quenching criterion

From both the theoretical and the observational sides, the separation between 'quenched' versus 'star-forming' galaxies is ambiguous and somewhat arbitrary. In this work, a specific star formation rate (sSFR) threshold of 10^{-11}yr^{-1} is employed to distinguish between quenched and star-forming galaxies. Unlike the star formation rate (SFR), which measures the absolute rate of star formation, the sSFR normalizes this rate by the total stellar mass of the galaxy, that is, $\text{sSFR} \equiv \text{SFR}/M_\star$. Galaxies with sSFR values below this threshold are considered quenched or quiescent, indicating a suppression of star formation activity, while those above are classified as actively star-forming.

Despite this threshold being adopted in the literature as a robust criterion for identifying quenched galaxies (e.g., Weinmann et al. 2010; De Lucia et al. 2012; Wetzel et al. 2013; Cecchi et al. 2019; Pallero et al. 2022), more sophisticated methods have been developed to classify galaxy quenching. For example, based on different criteria like deviation from the star forming main sequence (SFR vs. $M_\star$ plane), colour-colour cuts in the UVJ diagram, or redshift-sensitive sSFR thresholds (e.g., Furlong et al. 2015; Kuschel et al. 2023; Davé et al. 2019). However, there is no significant advantage in using these more refined criteria, as discussed in Donnari et al. (2019). Consequently, many studies have used the fixed sSFR threshold criteria due to its simplicity and effectiveness in identifying quenched populations. By using this threshold, not only do we ensure a clear distinction between quiescent and star-forming galaxies, but also we make our results directly comparable with the previously mentioned works.

General properties

In Figure 3.3, we plot the sSFR of the selected galaxies, illustrating the relationship with both lookback entry time (left) and stellar mass (right). It is important to emphasize that the sSFR values shown close to 10^{-14} are not actual data, as the simulation provides a null value for the sSFR below the resolution limit. To include these quenched subhaloes in the logarithmically scaled graph, we artificially assigned them a Gaussian distribution centred around 10^{-14}yr^{-1} with a standard deviation of $\sigma = 2 \times 10^{-15}\text{yr}^{-1}$. This approach allows us to estimate the number of subhaloes with null sSFR across entry snapshots by observing the spread of the distribution.

In the left panel plot, it is evident that the later subhaloes enter within the r_{200c} region, they tend to exhibit lower specific star formation rates (sSFR). This finding may be attributed to quenching events experienced by these subhaloes within distinct massive group structures prior to accreting into the central halo, following the hierarchical structure formation of the universe. This phenomenon is studied in depth in the section 3.4.2. In addition, a slightly unpopulated region can be found around 3 Gyrs in lookback time. This might be subjected to the virialization processes that undergo some clusters in the *Hydrangea* sample around this epoch. This processes not only can make clusters to stabilize their growth, but also they can start contracting their virial region, reducing the amount of galaxies that accrete into
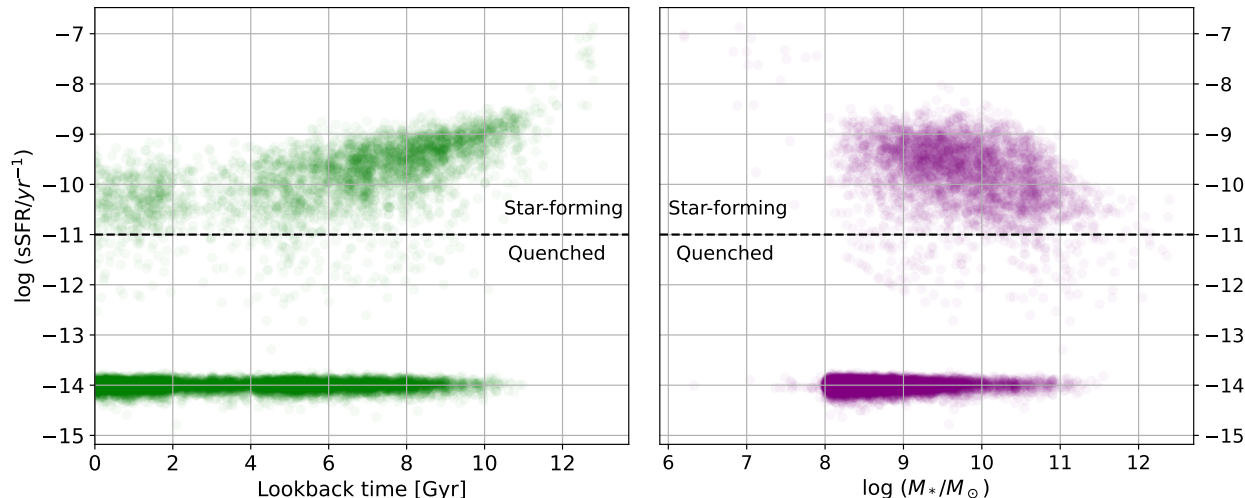
Figure 3.3: Scatter plots illustrating the relationship of sSFR with lookback time (left), and stellar mass (right). The dataset comprises all galaxies selected from each *Hydrangea* simulation run at their corresponding entry snapshot. The horizontal dashed line represents the sSFR threshold, separating star-forming and quiescent galaxies. sSFR values close to $10^{-14}\mathrm{yr}^{-1}$ are null data values that have been artificially assigned, sampling them with a Gaussian distribution centred around $10^{-14}\mathrm{yr}^{-1}$ with a standard deviation of $\sigma = 2 \times 10^{-15}\mathrm{yr}^{-1}$. The lookback time data has been smoothed to avoid a striped pattern as a result of the large time interval between most snapshots, convoluting it with a Gaussian distribution with a standard deviation of $\sigma = 0.4$ Gyrs.

the halo.

The right panel of Figure 3.3, reveals a notable negative correlation between the stellar masses of subhaloes at entry and their corresponding sSFR values. Specifically, subhaloes with larger stellar masses upon entry tend to exhibit a lower sSFR. This trend is often called the star-forming main sequence (rigorously speaking, it would be if we plotted the SFR vs. $M_\star$ plane), and may stem from factors such as larger feedback processes as the stellar masses of galaxies grow, e.g., the presence of a larger accreting black hole or the effects of supernova feedback from stars, both of which could contribute to the cessation of star-formation. We will eventually delve into these assumptions in a more detailed analysis, especially when it comes to the effects produced by the black holes, in section 3.4.1.

To categorize the entry status of galaxies, we examine whether they are actively forming stars or are no longer forming stars significantly when they first join the central cluster. In this context of galaxies accreting onto clusters, the 'processing' term is often used, in a sense that the clusters' environments processes the accreted galaxies, extinguishing their ability to renew their star population by forming new stars. So, we can separate our sample in pre- or post-processed galaxies, depending on their entry status. If they are already quenched at entry, we categorize them as pre-processed galaxies, while if they enter actively star forming, we classify them as post-processed galaxies, since they will eventually get quenched by the clusters' environment. Applying this categorization to the selected sample from all the *Hydrangea* runs, we detected a total of 9015 quenched galaxies upon entry into the observed region, constituting approximately 73% of the observed population. Conversely, there were 3336 star-forming galaxies detected at the time of entry, representing approximately 27% of the
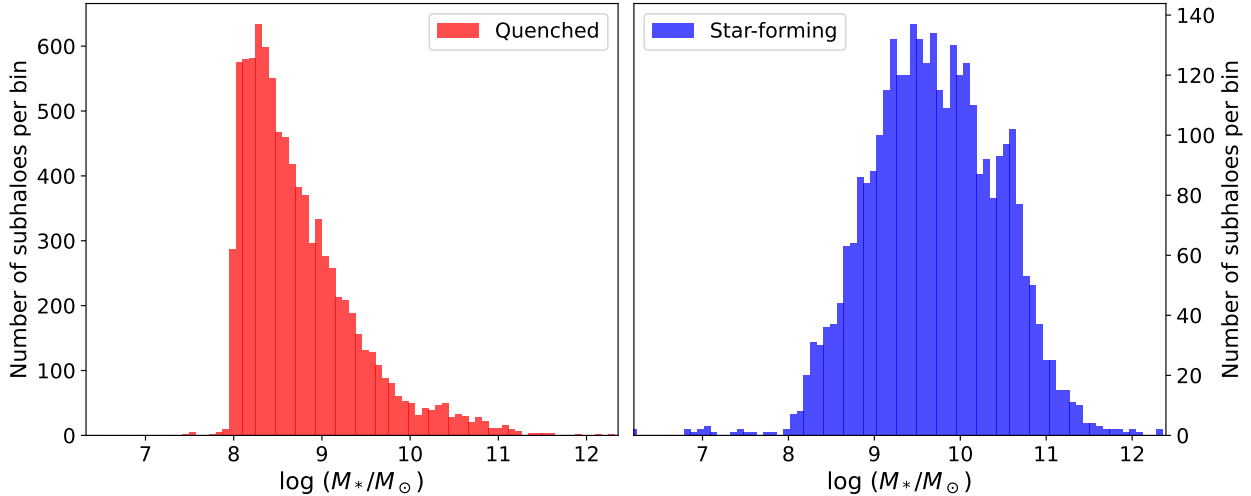
Figure 3.4: Stellar mass distributions of subhaloes at their entry snapshot. The left panel is for the quenched population upon entry (sSFR$< 10^{-11}$yr^{-1}), while the right one for the star-forming population (sSFR$> 10^{-11}$yr^{-1}). Note the different vertical scales.

total population under consideration.

Figure 3.4 shows the stellar mass distributions for both quenched and star-forming populations at the moment corresponding to their entry snapshot. In these plots, we see that the quenched population tends to have low masses upon entry, whereas their non-quenched counterparts exhibit a distribution more similar to a Gaussian distribution. As a consequence, even though the number of pre-processed subhaloes in our sample being larger than the post-processed ones, it does absolutely not represent the majority in terms of mass, since the high-mass subhaloes can contain up to 4 orders of magnitude more stellar mass. From this plot, it could be inferred that low-mass galaxies are more efficiently quenched outside the central cluster, perhaps undergoing pre-processing before even reaching r_{200c} or maybe as a result of other self-quenching mechanisms such as stellar feedback processes.

As galaxy mass increases, it becomes increasingly challenging for galaxies to undergo pre-processing. However, there is a slight peak observed around 10^{10} and 10^{11}, potentially indicating some massive galaxies that have been self-quenched or have been part of a large group before entering the central cluster. Regarding the star-forming population, low-mass galaxies are notably absent due to the prior quenching, while the most massive ones exhibit resistance to quenching. Nevertheless, this decay is also in part a consequence of the population of very high-mass galaxies being limited, resulting in a decrease in the quantity of these subhaloes as mass increases.

So far, we have seen the state at which subhaloes fall into the cluster. In this process, we noticed that the majority of the galaxies in our sample are already quiescent when they fall in, most of them being low-mass. Nonetheless, it would be beneficial to examine where these galaxies undergo quenching, to determine whether pre-processed galaxies are quenched by the main halo's environment beyond its virial region, or if other mechanisms are at play.
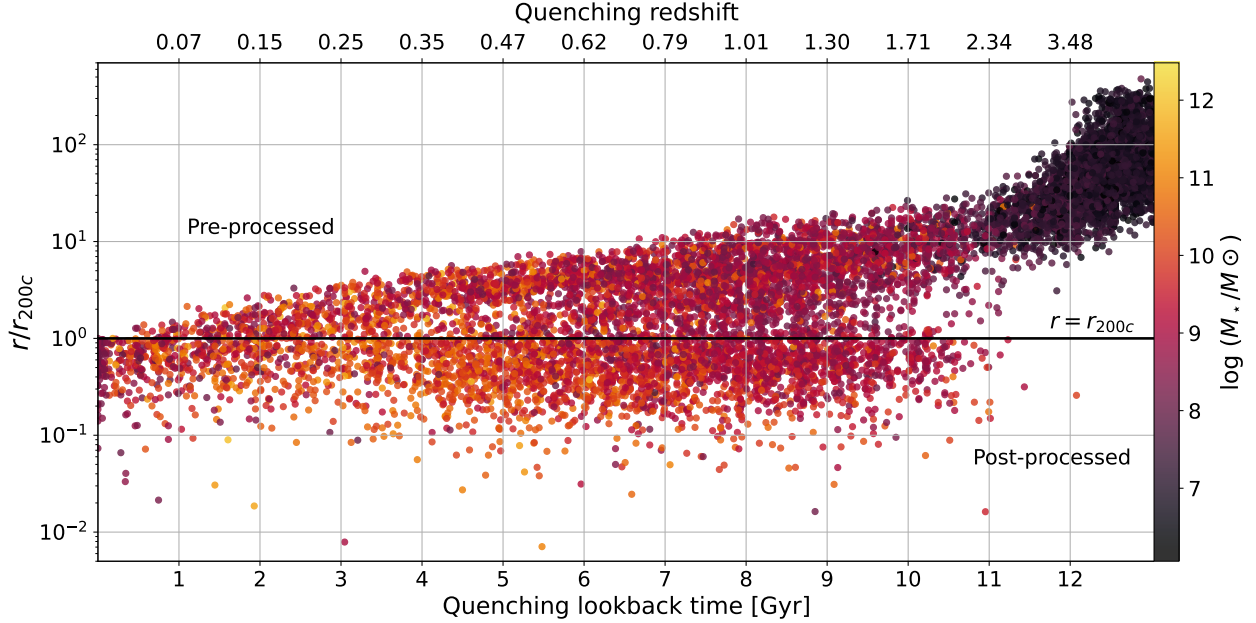
Figure 3.5: Quenching clusto-centric distance normalized with r_{200c} vs. time at which quenching happens, sSFR$< 10^{-11}$yr^{-1}, both in redshift (top) and in lookback time (bottom), for every subhalo selected in 3.1. The colormap indicates the stellar mass of these subhaloes at the moment they get quenched. The black horizontal line indicates the region at which $r = r_{200c}$, that is, the border of the virial region of the cluster. Hence, the points above this line belong to the pre-processed sample, and those below to the post-processed one. The time data has been smoothed for a better representation due to the low time resolution of the simulation, convoluting it with a Gaussian distribution with a standard deviation of $\sigma = 0.4$ Gyrs.

In order to study that, we select the quenching snapshots[2] for each subhalo in our sample and examine their positions relative to the main haloes in their respective simulations. Figure 3.5 shows the quenching distance versus the quenching time, in terms of redshift and lookback time, with a colour code representing their stellar mass content at that time, providing additional context.

From this plot, it is evident that a low mass galaxy population starts getting quiescent very early, within the first 2 Gyrs of the Universe, and at a high normalized clusto-centric distance [3], which is still a proto-cluster, and therefore does not influence these galaxies. As a consequence, it can be inferred that these dwarf galaxies are not getting quenched by the clustered environments, but by themselves, with different feedback mechanisms. However, this early quenching might not be entirely physical, since these dwarf galaxies lack sufficient stellar particles, causing the implemented subgrid physics to potentially fail, and quench them prematurely.

Despite this issue, a colour gradient can be observed, with higher mass galaxies quench-

---

[2]We define as quenching snapshot the first snapshot in which the target subhalo is already below the quenching threshold of sSFR$> 10^{-11}$yr^{-1}.

[3]The big values of r/r_{200c} in the right part of Figure 3.5 are due to the rapid grow of r_{200c} in the early stages of the universe. The maximum physical quenching clusto-centric distance is around 10 pMpc, since all selected subhaloes will be inside r_{200c} at $z = 0$.

ing later and closer to the main halo. This can be for two reasons; firstly, the hierarchical formation of galaxies results in the majority of high-mass galaxies forming at later stages. Secondly, massive galaxies continuously accrete smaller galaxies, thereby replenishing their gas content and subsequently delaying their quenching processes. Nonetheless, there is a significant dispersion in stellar mass (excluding the dark region in the top-right part), indicating that quenching processes are diverse and not strictly mass-dependent.

Another major conclusion is the presence of a horizontal band just below the black line, representing the border of the virial region. This suggests that this virial region delimited by r_{200c} is a good choice to make an approximate and qualitative distinction between those galaxies that are processed by the main halo (post-processed) and those that are not (pre-processed), given that a considerable population of galaxies gets quenched right after crossing that border, surely due to the environmental effects. When it comes to this fraction of quenched galaxies by the central cluster's environment, they will be further explored in section 3.5.

Apart from that, the observed diagonal tendency is a consequence of the selection of our sample, since we chose those galaxies that end up inside the central cluster at $z = 0$, and thus, galaxies have to be nearer the border when lookback time gets smaller. Irrespective of the reason, it can be concluded that the quenching of galaxies in the diagonal band above the line is not due to the central cluster's environment, but rather other mechanisms, which will be discussed in detail in section 3.4.

Galaxy rejuvenation

Up to this point, our analysis has implicitly assumed that a galaxy remains inactive once it crosses the quenching threshold of sSFR $< 10^{-11}\mathrm{yr}^{-1}$. Nevertheless, theoretically, a galaxy might resume its star-formation activity and rejuvenate its stellar population, although this should only happen in remote cases (Poggianti et al. 2019).

Hence, we conduct an examination of the simulated data to ensure its accuracy. This check is aimed to confirm that galaxies entering the central cluster environment in a quenched or pre-processed state do not undergo any significant rejuvenation processes, and if they did, to rule them out of our selection, given that they are not relevant for our objectives.

We track galaxies that enter the central cluster already in a quenched state (sSFR $< 10^{-11}\mathrm{yr}^{-1}$). Then, we monitor their evolution over time to see if any of these galaxies experience a resurgence in star formation activity (sSFR $> 10^{-11}\mathrm{yr}^{-1}$) once inside the cluster environment.

The results of our analysis yield a reassuring outcome: no significant quantity of subhaloes show evidence of rejuvenation within the central cluster. Only 6 subhaloes were found to be rejuvenating in the entire selection of the *Hydrangea* sample, which is truly insignificant due to the vast quantity of subhaloes present in these runs. When it comes to these special cases, they could very well be a result of mergers, due to how the merger tree is computed. For example, when a smaller star forming subhalo joins a heavier quenched halo, the ID of the most massive quenched halo is conserved on the merger tree, and thus, the resulting galaxy has a composite stellar population that is not due to an in-situ star-formation, but a merger. This insignificant quantity of rejuvenated subhaloes provides confidence in the reliability of our simulated data and the accuracy of our methodology, including the subhalo finder and

the merger tree used. Hence, we conclude that no further restriction has to be applied to the selected sample given the insignificant amount of rejuvenated galaxies found.

In the following sections, we dive into the data more thoroughly, with the aim of looking for causes of the physical processes responsible for the quenching.

3.4 Pre-processed galaxies

In this section, we will examine the galaxies that enter the cluster in a pre-processed state, accounting for 73% of our sample. As seen in Figure 3.4, this pre-processed sample is mainly dominated by low-mass subhaloes and as a consequence, even though the percentage being dominant, it absolutely does not represent the majority in terms of mass.

It is believed that the predominant processes associated with this early quenching may be self-quenching or even the processing in its own halo. In the following lines, we probe which mechanisms are responsible for this, and which is their relative degree of importance.

3.4.1 Self-quenching

Self-quenching refers to the phenomenon where a galaxy becomes quiescent through an internal process, independent of any interaction with its external environment. These processes mainly tend to be a consequence of feedback processes, such as stellar feedback (provided by supernovae when stars die) or AGN feedback (provided by activity of supermassive black holes). Depending on the mass of the galaxy, one will dominate over the other. For low-mass galaxies, stellar feedback will be the dominant mechanism, since these galaxies will not host a sufficiently massive black hole for the AGN feedback to be efficient. Nevertheless, for those galaxies hosting a supermassive black hole (intermediate- and high-mass galaxies), AGN feedback will certainly dominate over the stellar feedback (Talbot et al. 2021).

Having said that, we focus our self-quenching analysis on the effects produced by the SMBHs that reside in the central regions of our sample galaxies (53.63% of the selected preprocessed galaxies host a central SMBH). To do so, we examine how the star-forming activity correlates with the BH accretion rate. Data for this analysis is taken from the procedures described in sections 2.4 and 2.5.

In Figure 3.6, three example subhaloes are shown for a highly correlated star-formation quenching with BH activity, plotting the central SMBH accretion rate and SFR vs. lookback time. In the top one, an abrupt cessation in star formation activity is visible, at the same time with the quasar burst of the central SMBH. In the mid one, two peak in star formation activity are visible. The decrease of the first one is not correlated with the AGN activity, but the second one decreases impulsively in response to quasar mode bursts. In the bottom one, a more gradual decline can be seen, given that quasar mode bursts of its central SMBH are not that strong.

This analysis is done by cross-matching the BH IDs with the subhalo IDs generated by the subhalo finder in order to know which subhalo is the one hosting the SMBH. However, the problem with this procedure is that we have a large sample of galaxies to examine, and hence we cannot scrutinize them individually as we do in Figure 3.6. Thus, we have to approach this differently. For this purpose, we define two quantities that are proxies for AGN feedback.
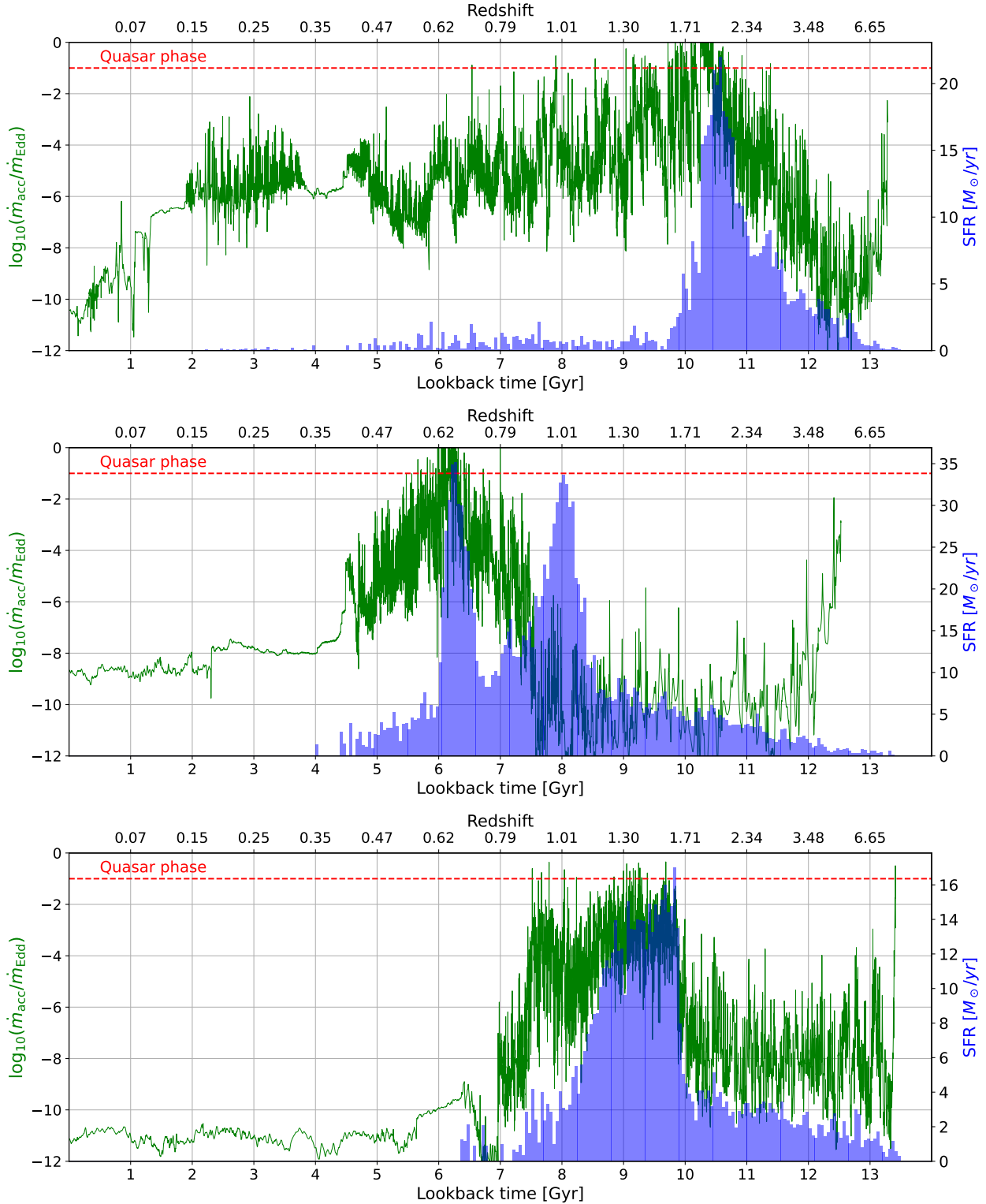
Figure 3.6: Examples of black hole Eddington ratio (green) and star-formation rate (blue) time evolution. These three galaxies are selected as representative examples of subhaloes with a high time correlation of star-forming discontinuance with AGN activity. They belong to run CE-29 at $z = 0$, and their IDs are 591, 211, and 438, in descending order. The red horizontal dashed line indicates the $\lambda = 0.1$ threshold adopted for the Eddington ratio to be considered in quasar mode.
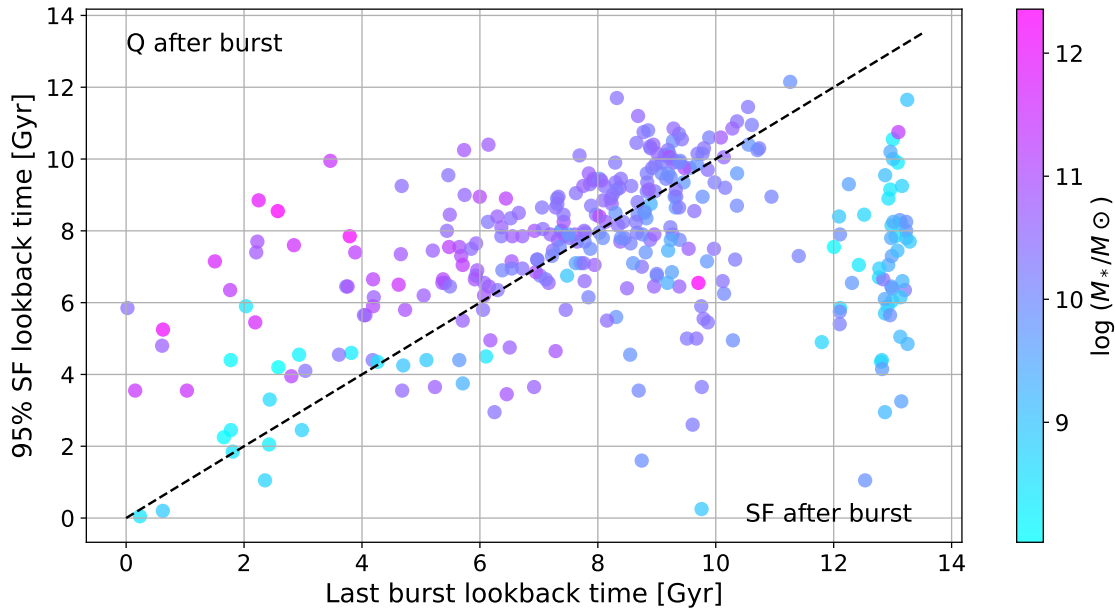
Figure 3.7: Time of 95% star formation vs. last quasar burst time for all the pre-processed subhaloes that undergo a quasar phase before entering the central cluster for the selected sample. The diagonal dashed line provides the perfect correlation. The points located above, have formed 95% of stellar mass before the last burst, thus they are quenched after last burst, while the ones below keep forming more than a 5% of their stellar mass content after the last AGN burst, thus they keep star-forming after last burst. The colorbar represents their stellar mass content at their entry snapshot.

On the one hand, by performing a cumulative sum of a SFH, we calculate the time when a subhalo has formed 95% of the total stellar mass created in its life span. This way, we obtain a time value at which nearly all the stellar mass has already been generated by the subhalo. On the other hand, we compute the last time when the SMBH accretion rate is above $\lambda = 0.1$ (happens in 16.56% of subhaloes with central SMBH), for which we consider a quasar-mode burst. Thus, we record the final quasar-mode accretion burst event in lookback time for that specific subhalo. Now, we can collectively investigate the relationship between the cessation of star-formation activity and black hole activity. This allows us to determine whether subhaloes continue to form stars following the last burst (indicating no correlation) or if this burst (or an earlier one) could be the cause for galaxies to become quiescent.

Figure 3.7 illustrates that close to half (47.79%) of the subhaloes experiencing quasar bursts continued star forming after the last central SMBH quasar outburst. This implies that the remaining half's quenching could be linked to these quasar bursts, suggesting that it is likely for them to get suppressed by the AGN feedback. When it comes to the types of galaxies we encounter in each region, we see that the largest galaxies usually get quenched way before the last burst, probably because of a larger central SMBH quenching the galaxy very effectively within the first quasar-mode bursts. In contrast, some of the lightest galaxies have slightly correlated and recent star formations and bursts, whereas others have a very early burst, not affecting their star formation activity. This is probably due to relatively small SMBHs, which are not able to quench their host galaxies. Hence, these last low-mass galaxies show no correlation between SHF and AGN feedback, locating vertically on the

right side of the plot. Those galaxies with intermediate masses are generally present near and above the perfect correlation line, showing that probably the last quasar-mode bursts of the AGNs are responsible for their cessation in star-forming activity.

3.4.2 Processing in its own group halo

Another significant mechanism is thought to be the processing in its own halo. This suggests that prior to its integration into the central FOF group, it was part of a considerably large FOF group, which was likely capable of quenching the subhaloes within it, much like the central cluster, albeit on a smaller scale.

To investigate this phenomenon, we consider the set of pre-processed subhaloes whose cessation of star formation does not correlate with the black hole activity, or even those that do not have an AGN. For these subhaloes, we monitor the FOF group M_{200c} at the snapshot before they become part of the central cluster, that is, the last snapshot when GroupNumber $\neq 1$. In this way, we determine the size of their galaxy groups prior to their incorporation into the main halo. Figure 3.8 shows the distribution of previous group masses, M_{200c}, for all the pre-processed subhaloes selected from the *Hydrangea* sample.
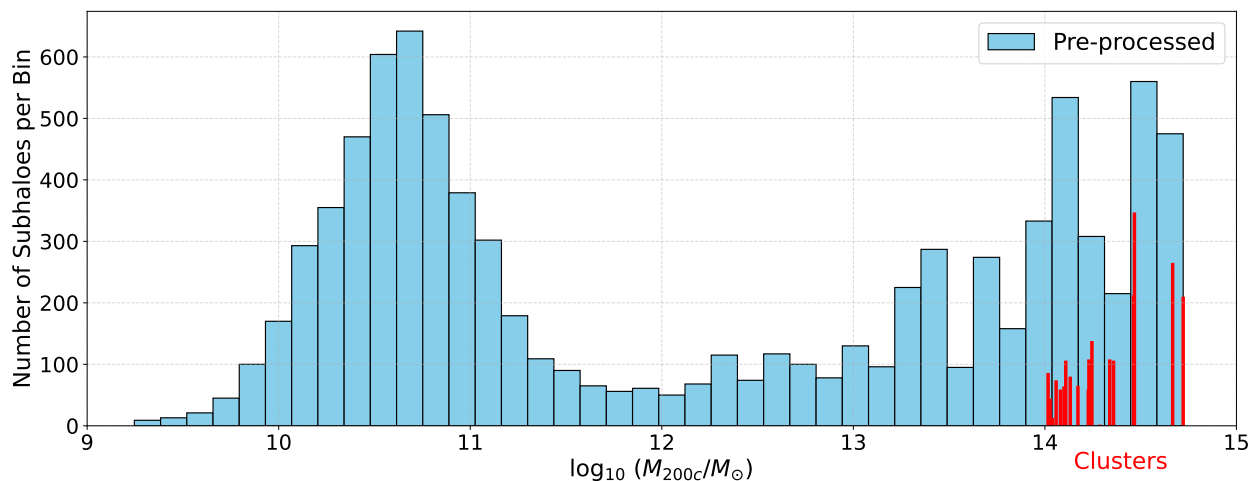

Figure 3.8: Group M_{200c} histogram for all the pre-processed subhaloes selected from the *Hydrangea* sample. The group mass values for each subhalo are taken at the snapshot previous to joining the main FOF group. The red bars at $M_{200c} > 10^{14} M_\odot$ represent the contribution is highly dominated by mergers, each line representing a cluster previous to joining the central, and the length of it being proportional to the amount of subhaloes in that cluster.

This plot illustrates that the majority of the subhaloes come from groups where $10^{10} M_\odot < M_{200c} < 10^{11} M_\odot$. Furthermore, a significant number of subhaloes are derived from very massive FOF structures, with some of them even qualifying as galaxy clusters, as their M_{200c} exceeds $10^{14} M_\odot$ (represented by the red bars in Figure 3.8). In fact, around 25% of the subhaloes entering the central halo come from groups where $M_{200c} > 10^{14} M_\odot$. This implies that subhaloes coming from these or similarly sized groups have experienced processing similar to what they would have undergone inside the central halo, due to their previous exposure to high-density environments. These large groups contribute to substantial mergers between

cluster structures, resulting in larger formations, as seen in some of the heaviest runs of the *Hydrangea* sample. Consequently, the processing mechanism of these subhaloes that originate from large groups is expected to be similar to that of the subhaloes that we will examine in the following section 3.5.

3.5 Post-processed galaxies

In this section, we will examine the galaxies that enter the cluster while star forming, which is around the 27% of the subhaloes in our selection. In spite of being the minority in number, they contain most of the stellar mass of the final cluster, since this percentage contains most of the intermediate and high mass galaxies. The vast majority of these galaxies will eventually be processed by the effects produced by the dense environment. In fact, at $z = 0$, only around 18% of the galaxies catalogued as post-processed are still star forming, although being inside the high density virial region of the central cluster. We attribute this percentage to the galaxies entering the cluster at low redshift. Consequently, we consider that insufficient time has passed to cease their star forming activity effectively, but they will eventually have the same fate.

It has been known for decades that the galaxies entering the virial radius of a cluster tend to become quenched faster than in field (Dressler 1980). In recent works as Pallero et al. (2022), it has been seen that in C-EAGLE, the majority of galaxies that entered the virial radius of a cluster became quenched within a time interval of a Gyr. This is mainly attributed to a physical process called ram pressure stripping (see 3.5.1). Nevertheless, there are other potential mechanisms, including tidal effects, that have been considered accountable for this process. The tidal effects would not only strip gas from galaxies but would also remove stars and dark matter. However, recent works have concluded that its influence is not comparable to the ram pressure stripping in EAGLE simulations (e.g., Marasco et al. 2016; Kulier et al. 2023), specially for the most massive groups ($M_{200c} > 10^{14}$ M$_\odot$). Since our simulations are centred on clusters (refer to Table 2.1 for details), we focus mainly on ram pressure stripping as the main environmental mechanism responsible for quenching galaxies.

3.5.1 Ram pressure stripping

Ram pressure stripping consists of the removal of gas from infalling galaxies due to the pressure created by their motion relative to the group or cluster medium, first described in Gunn & Gott III (1972). It can be seen as if the cluster's environment is too dense to go through for the gas contained in the galaxies, getting stripped away and left behind, as their host galaxy continues its infall. This gas removal occurs when the ram pressure force surpasses the gravitational potential's restoring force acting on the gas. Ram pressure is proportional to the intracluster medium (ICM) density, as well as the square of the relative velocity between the infalling galaxy and the intracluster medium, $P_{\mathrm{ram}} = \rho_{\mathrm{ICM}} v_{\mathrm{rel}}^2$. As a result, galaxies experiencing infall into clustered high density environments get gas stripped and strangulated out of fuel to form stars, particularly from its outer regions where the gravitational binding is weaker. The gas is left behind, forming long gaseous tails that can be observed in the ICM (Poggianti et al. 2019).
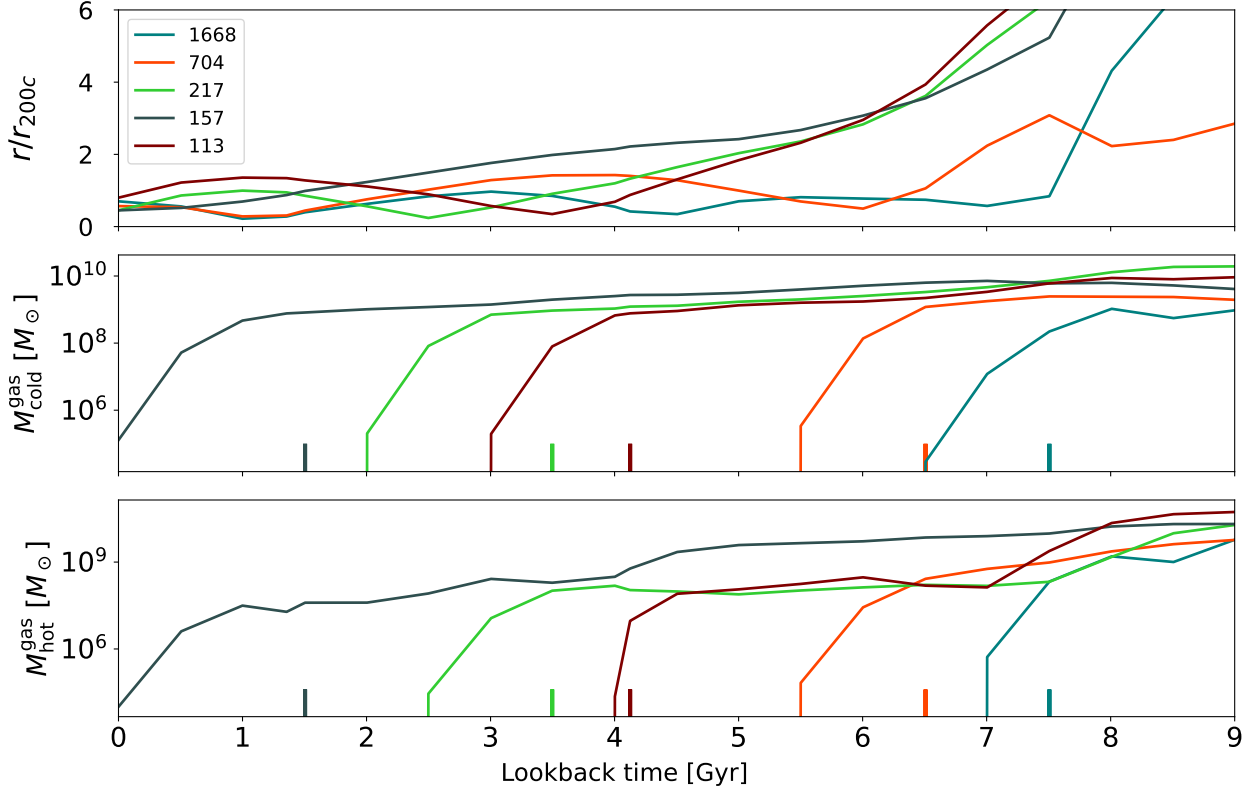
Figure 3.9: Time evolution of normalized clusto-centric distance (top panel), cold gas content (central panel) and hot gas content (bottom panel), for five randomly selected subhaloes from run CE-29. Each colour represents a subhalo, whose $z = 0$ ID is shown in the legend. The vertical coloured bars represent the time at which each subhalo enters the r_{200c} region. The data has been smoothed for a better representation due to the low time resolution of the simulation, convoluting it with a Gaussian distribution with a standard deviation of $\sigma = 0.5$ Gyrs.

To begin with our analysis, we start looking at the impact caused by ram pressure stripping. For this purpose, we randomly selected 5 post-processed subhaloes from the largest run, CE-29, and monitored the changes in their cold/neutral and hot/ionized gas compositions as they fall into the central cluster (Figure 3.9).

From Figure 3.9, it is evident that both cold star forming and hot gas contents start to get depleted right after they enter the virial region of the central cluster. In this case, we are mostly interested in the cold neutral plotted in the central panel, since it is the one that is able to form stars. Nevertheless, we complement it with the ionized hot gas content, since it could happen that the gas could be heating as a consequence of a feedback process and not getting stripped away. However, note that the hot gas content is not increasing, but is also drastically reduced. Hence, the percentage of cold gas being heated up into hot gas by feedback is negligible, and we conclude that the gas is getting stripped away regardless of its temperature.

In order to analyse the full sample of post-processed galaxies, we consider a subhalo as gas depleted if its gas mass falls below 10% of their stellar mass content, that is, if $M_{\rm gas}/M_\star < 0.1$. We implement this instead of checking against a fixed gas mass threshold,
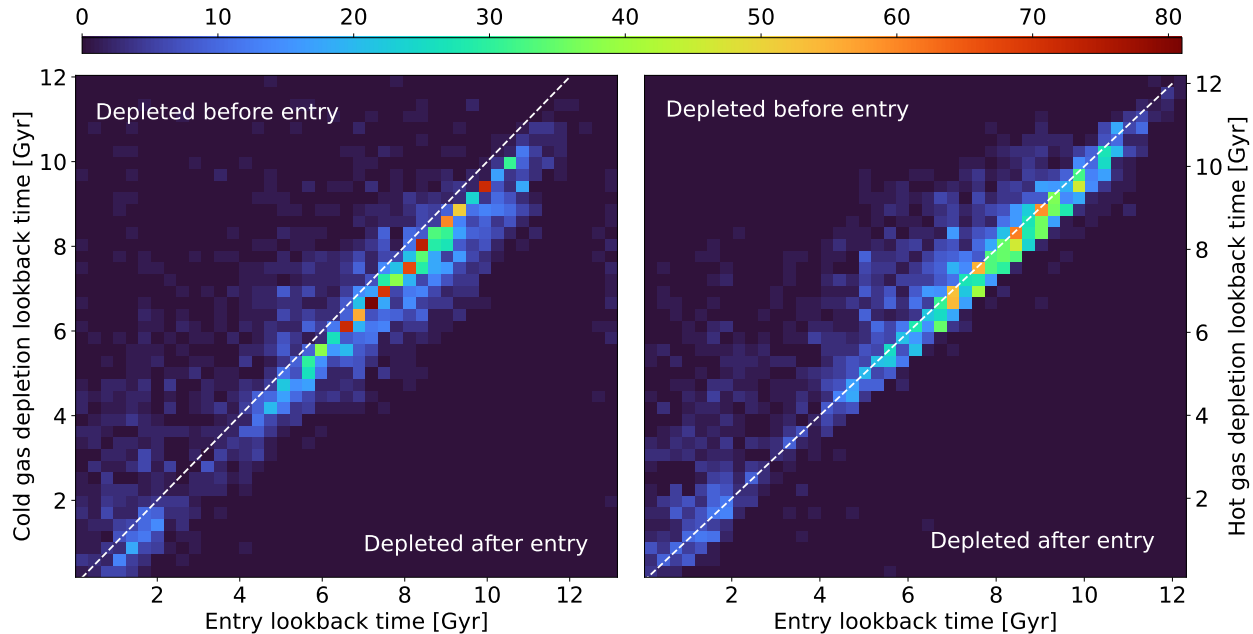
Figure 3.10: 2D histograms for the time at which gas contents get depleted ($M_{\mathrm{gas}}/M_{\star} < 0.1$) vs. the time those galaxies enter the virial region of the central cluster ($r < r_{200c}$), in lookback time. In the left panel, the cold star-forming gas content is represented, while in the right the hot non-star-forming one. The diagonal white dashed line shows the perfect correlation between the gas content depletion time and entry time variables. The galaxies located above this line, have depleted their cold gas before entering the central cluster, while the ones below the line get depleted after the incorporation. The data in both axis has been convolved with a Gaussian distribution with a standard deviation of $\sigma = 0.4$ Gyrs. The colormap indicates the number of subhaloes in each bin.

to overcome the fact not every galaxy enters with the same amount of gas, since massive galaxies containing large gas reservoirs would need further stripping to get considered as depleted. This approach allows for a more precise representation of stripping, considering that it is dynamically determined based on the stellar mass of each subhalo.

Figure 3.10 shows the depletion time vs. the entry time for each post-processed subhalo that gets depleted in our sample. The depletion times are calculated as the times when gas contents of a galaxy are below $0.1 \times M_{\star}$ for the first time after reaching their maximum gas content value. This last step is taken because initially a galaxy could be depleted of cold gas, but eventually generate cold gas by cooling their gas content, or incorporate gas with other processes as mergers.

In the left panel of Figure 3.10, one can see that the vast majority of galaxies are depleted in cold gas right after entering the central cluster. However, a substantial amount of them take a couple of Gyrs to get depleted after entry, which could be due to different effects that hold back gas depletion. For example, some gas-rich galaxies can be shielded from ram pressure by other dense regions, as found in Roediger & Brüggen (2007) and Jáchym et al. (2009), or even ram pressure can induce spiral waves in the gas that transport angular momentum outward, leading to the contraction of the inner part of the galaxy and preventing further stripping, as discussed in Schulz & Struck (2001). Apart from that, a minor proportion of

galaxies appear to be depleted in cold gas before even entering the central cluster. The ones that get depleted right before entry could very well be a consequence of lower ram pressure strippings being able to deplete some subhaloes, but still some of them are clearly not a consequence of this effect. We roughly estimated the fraction of these subhaloes as a 2%, with the condition of getting depleted in cold gas 4 Gyrs before entering the central cluster. A possible explanation for those galaxies substantially above from the perfect correlation line is that they have probably undergone a slow starvation process. In this process, the galaxy slowly consumes their cold gas reservoir, until no more fuel is left to keep forming stars[4]. This is supported by the fact that those subhaloes in the top left part of the cold gas panel get depleted in cold gas but take longer to get depleted in hot gas, suggesting that the responsible mechanism is only consuming cold gas. This commonly happens to isolated satellite galaxies that do not have undergone mergers, since these mergers can enrich their gas content and, in this manner, be able to keep forming stars (Park et al. 2023).

Something very similar to the cold gas panel can be seen in the right panel, referring to the hot gas content, since a large proportion of the galaxies get depleted in hot gas immediately after entry. This tells us that it is in fact the ram pressure stripping what is eliminating the gas in those cases, and not that the gas is getting heated and ionized. However, it can be appreciated that a significant quantity of hot gas depletions occur a Gyr or two before entry, suggesting that ram pressure stripping is slightly more efficient in hot gas compared to cold gas. This can also be seen from Figure 3.9, where the randomly selected sample of galaxies usually get depleted faster in hot gas than in cold gas. This result is in accordance with Kulier et al. (2023), where it is stated that the ionized (hot) gas can be stripped by lower ram pressures than the neutral (cold) one, after calculating ram pressure values on a toy model. For the same reason, we do not detect a considerable amount of subhalos getting depleted of hot gas a few Gyrs after entry, in contrast with what we see for the cold gas panel.

---

[4]Note that some galaxies are considered star forming (sSFR$> 10^{-11}$yr^{-1}) at entry (post-processed), but also they are considered depleted ($M_{\mathrm{gas}}/M_\star < 0.1$) before entering. This is due to how we define depletion, since depleted galaxies can still keep forming stars slowly.

4 | Conclusions

This work investigates the quenching mechanisms that suppress star formation in galaxies within galaxy clusters and their vicinities, using state-of-the-art cosmological hydrodynamical simulations from the Cluster-EAGLE (C-EAGLE) (Barnes et al. 2017) project. The analysis focuses on examining the properties and evolution of galaxies as they accrete onto the main cluster halo, with the aim of identifying the dominant physical processes responsible for quenching their star formation activity.

We selected a sample of galaxies accreting onto the central cluster halo from the *Hydrangea* sample simulations, categorized as either "pre-processed" (quenched before accretion) or "post-processed" (star-forming at accretion). Various properties of these galaxies were analyzed, including star formation histories, black hole accretion rates, and gas content evolution. Correlations between these properties were examined to identify potential quenching mechanisms.

The key findings of this can be summed up in the following points:

- Environmental quenching mechanisms play a critical role in suppressing star formation in galaxies within galaxy clusters. The colour-stellar mass diagram (Figure 3.2) clearly shows a distinct lack of blue, star-forming galaxies within the virial radius of the central cluster, indicating that these galaxies have been efficiently quenched by the dense cluster environment. Also, this demonstrates that the simulations accurately reproduce the observed colour-mass relation, as discussed in Negri et al. (2022), with a prominent red sequence of quenched galaxies within the cluster virial region and a more extended blue cloud of star-forming galaxies in the outskirts, consistent with observational data.

- The analysis of the properties of galaxies accreting onto the main cluster halo reveals that a significant fraction (around 73%) of these galaxies were already quenched (pre-processed) before entering the virial radius. For these pre-processed galaxies, the main quenching mechanisms identified are:

  - Self-quenching due to AGN feedback: For around half of the pre-processed galaxies with central supermassive black holes (SMBHs), the cessation of star formation is well correlated with the final quasar-mode accretion burst from the active galactic nucleus (AGN) (Figure 3.7).

  - Processing in their own group halo: Many pre-processed galaxies (around 25%) originated from massive galaxy groups (with $M_{200c} > 10^{14}M_\odot$) before accreting onto the main cluster (Figure 3.8). The high-density environment within these

31

massive groups likely facilitated quenching processes similar to those occurring within the central cluster itself.

- For the remaining 27% of galaxies that were still star-forming when accreting onto the main cluster halo (post-processed), the primary quenching mechanism identified is ram pressure stripping. This process efficiently removes the cold gas reservoir required for star formation from galaxies shortly after entering the dense intracluster medium within the virial radius (Figure 3.10).

- A small fraction of cold gas depleted galaxies (around 2%) exhibited a slow starvation process, gradually consuming their cold gas reservoir before accretion, potentially due to isolation from gas-rich mergers. Nevertheless, our findings indicate that this has a comparatively unimportant impact.

- Tidal effects produced by the clusters were considered to play a relatively minor role in quenching galaxies within these simulations compared to ram pressure stripping and self-quenching mechanisms (Marasco et al. 2016; Kulier et al. 2023).

- The efficiency of quenching processes is found to be mass-dependent. Lower mass galaxies are more prone to be pre-processed and quenched before they even reach the central regions of the cluster. Higher mass galaxies, on the other hand, are more resistant to quenching, probably due to constant gas accretions, and often require the dense environment of the cluster core to halt their star formation.

- The relative importance of the identified quenching mechanisms varies depending on the specific properties and histories of individual galaxies, such as their mass, their merging history or their environment's evolution, highlighting the complex interplay of various physical processes.

Overall, the results demonstrate the capability of state-of-the-art cosmological simulations to capture the complex interplay between various quenching mechanisms, providing valuable insights into the environmental processes that shape galaxy evolution within the extreme environments of galaxy clusters. Furthermore, it has been shown that galaxy clusters are extremely efficient environments for quenching star formation in the galaxies that merge into them.

Ram pressure stripping emerges as the dominant mechanism of environmental quenching, which is the main mechanism responsible for quenching galaxies after they have accreted onto the clustered haloes. On the other hand, we have highlighted AGN feedback as one of the mechanisms playing a crucial role in pre-processing galaxies before they enter the clusters.

Bibliography

Bahé Y. M., McCarthy I. G., 2015, Monthly Notices of the Royal Astronomical Society, 447, 969

Bahé Y. M., McCarthy I. G., Balogh M. L., Font A. S., 2013, Monthly Notices of the Royal Astronomical Society, 430, 3017

Bahé Y. M., et al., 2017, Monthly Notices of the Royal Astronomical Society, 470, 4186

Bahé Y. M., et al., 2019, Monthly Notices of the Royal Astronomical Society, 485, 2287

Baldry I. K., Balogh M. L., Bower R., Glazebrook K., Nichol R. C., Bamford S. P., Budavari T., 2006, Monthly Notices of the Royal Astronomical Society, 373, 469

Barnes D. J., Kay S. T., Henson M. A., McCarthy I. G., Schaye J., Jenkins A., 2016, Monthly Notices of the Royal Astronomical Society, p. stw2722

Barnes D. J., et al., 2017, Monthly Notices of the Royal Astronomical Society, 471, 1088

Behroozi P. S., Wechsler R. H., Wu H.-Y., 2012, The Astrophysical Journal, 762, 109

Blanton M. R., Moustakas J., 2009, Annual Review of Astronomy and Astrophysics, 47, 159

Blanton M. R., et al., 2005, The Astronomical Journal, 129, 2562

Bondi H., Hoyle F., 1944, Monthly Notices of the Royal Astronomical Society, 104, 273

Bower R. G., Benson A., Malbon R., Helly J., Frenk C., Baugh C., Cole S., Lacey C., 2006, Monthly Notices of the Royal Astronomical Society, 370, 645

Cecchi R., Bolzonella M., Cimatti A., Girelli G., 2019, The Astrophysical Journal Letters, 880, L14

Chabrier G., 2003, Publications of the Astronomical Society of the Pacific, 115, 763

Contini E., Gu Q., Kang X., Rhee J., Yi S., 2019, The Astrophysical Journal, 882, 167

Contini E., Gu Q., Ge X., Rhee J., Yi S., Kang X., 2020, The Astrophysical Journal, 889, 156

Cora S. A., et al., 2018, Monthly Notices of the Royal Astronomical Society, 479, 2

Crain R. A., et al., 2015, Monthly Notices of the Royal Astronomical Society, 450, 1937

Croton D. J., et al., 2006, Monthly Notices of the Royal Astronomical Society, 365, 11

Davé R., Anglés-Alcázar D., Narayanan D., Li Q., Rafieferantsoa M. H., Appleby S., 2019, Monthly Notices of the Royal Astronomical Society, 486, 2827

De Lucia G., Weinmann S., Poggianti B. M., Aragon-Salamanca A., Zaritsky D., 2012,

Monthly Notices of the Royal Astronomical Society, 423, 1277

Dolag K., Borgani S., Murante G., Springel V., 2009, Monthly Notices of the Royal Astronomical Society, 399, 497

Donnari M., et al., 2019, Monthly Notices of the Royal Astronomical Society, 485, 4817

Donnari M., Pillepich A., Nelson D., Marinacci F., Vogelsberger M., Hernquist L., 2021, Monthly Notices of the Royal Astronomical Society, 506, 4760

Dressler A., 1980, Astrophysical Journal, Part 1, vol. 236, Mar. 1, 1980, p. 351-365., 236, 351

EAGLE-Team 2017, arXiv [Pre-prints]

Eisenstein D. J., et al., 2011, The Astronomical Journal, 142, 72

Fujita Y., 2004, Publications of the Astronomical Society of Japan, 56, 29

Furlong M., et al., 2015, Monthly Notices of the Royal Astronomical Society, 450, 4486

Girardi L., Bressan A., Bertelli G., Chiosi C., 2000, VizieR Online Data Catalog, pp J–A+

Gomez P. L., et al., 2003, The Astrophysical Journal, 584, 210

Gunn J. E., Gott III J. R., 1972, Astrophysical Journal, vol. 176, p. 1, 176, 1

Häring N., Rix H.-W., 2004, The Astrophysical Journal, 604, L89

Henriques B. M., White S. D., Thomas P. A., Angulo R. E., Guo Q., Lemson G., Wang W., 2017, Monthly Notices of the Royal Astronomical Society, 469, 2626

Hogg D. W., et al., 2003, The Astrophysical Journal, 585, L5

Jáchym P., Köppen J., Palouš J., Combes F., 2009, Astronomy & Astrophysics, 500, 693

Kauffmann G., White S. D., Heckman T. M., Ménard B., Brinchmann J., Charlot S., Tremonti C., Brinkmann J., 2004, Monthly Notices of the Royal Astronomical Society, 353, 713

Kormendy J., Ho L. C., 2013, Annual Review of Astronomy and Astrophysics, 51, 511

Kulier A., et al., 2023, The Astrophysical Journal, 954, 177

Kuschel M., et al., 2023, The Astrophysical Journal, 947, 17

Marasco A., Crain R. A., Schaye J., Bahé Y. M., van der Hulst T., Theuns T., Bower R. G., 2016, Monthly Notices of the Royal Astronomical Society, 461, 2630

McAlpine S., et al., 2016, Astronomy and computing, 15, 72

Mok A., et al., 2014, Monthly Notices of the Royal Astronomical Society, 438, 3070

Moran S. M., Ellis R. S., Treu T., Smith G. P., Rich R. M., Smail I., 2007, The Astrophysical Journal, 671, 1503

Negri A., Dalla Vecchia C., Aguerri J. A. L., Bahé Y., 2022, Monthly Notices of the Royal Astronomical Society, 515, 2121

Onions J., et al., 2012, Monthly Notices of the Royal Astronomical Society, 423, 1200

Pallero D., Gómez F. A., Padilla N. D., Torres-Flores S., Demarco R., Cerulo P., Olave-Rojas D., 2019, Monthly Notices of the Royal Astronomical Society, 488, 847

Pallero D., Gómez F. A., Padilla N. D., Bahé Y. M., Vega-Martínez C. A., Torres-Flores S.,

2022, Monthly Notices of the Royal Astronomical Society, 511, 3210

Park M., et al., 2023, The Astrophysical Journal, 953, 119

Planck Collaboration P., et al., 2014, A&A, 571, A16

Poggianti B. M., et al., 2006, The Astrophysical Journal, 642, 188

Poggianti B. M., et al., 2019, The Astrophysical Journal, 887, 155

Postman M., Geller M., 1984, Astrophysical Journal, Part 1 (ISSN 0004-637X), vol. 281, June 1, 1984, p. 95-99., 281, 95

Qu Y., et al., 2017, Monthly Notices of the Royal Astronomical Society, 464, 1659

Rodriguez-Gomez V., et al., 2015, Monthly Notices of the Royal Astronomical Society, 449, 49

Roediger E., Brüggen M., 2007, Monthly Notices of the Royal Astronomical Society, 380, 1399

Schaye J., et al., 2015, Monthly Notices of the Royal Astronomical Society, 446, 521

Schulz S., Struck C., 2001, Monthly Notices of the Royal Astronomical Society, 328, 185

Sijacki D., Springel V., Di Matteo T., Hernquist L., 2007, Monthly Notices of the Royal Astronomical Society, 380, 877

Smith B. D., Lang M., 2019, Journal of Open Source Software, 4, 1881

Springel V., 2005, Monthly notices of the royal astronomical society, 364, 1105

Springel V., White S. D., Tormen G., Kauffmann G., 2001, Monthly Notices of the Royal Astronomical Society, 328, 726

Stevens A. R., Brown T., 2017, Monthly Notices of the Royal Astronomical Society, 471, 447

Talbot R. Y., Bourne M. A., Sijacki D., 2021, Monthly Notices of the Royal Astronomical Society, 504, 3619–3650

Taylor P., Federrath C., Kobayashi C., 2017, Monthly Notices of the Royal Astronomical Society, 469, 4249

Tormen G., Bouchet F. R., White S. D., 1997, Monthly Notices of the Royal Astronomical Society, 286, 865

Trayford J. W., et al., 2015, Monthly Notices of the Royal Astronomical Society, 452, 2879

Vazdekis A., Koleva M., Ricciardelli E., Röck B., Falcón-Barroso J., 2016, Monthly Notices of the Royal Astronomical Society, 463, 3409

Vogelsberger M., Marinacci F., Torrey P., Puchwein E., 2020, Nature Reviews Physics, 2, 42

Weinmann S. M., Kauffmann G., Von Der Linden A., De Lucia G., 2010, Monthly Notices of the Royal Astronomical Society, 406, 2249

Wetzel A. R., Tinker J. L., Conroy C., Van Den Bosch F. C., 2013, Monthly Notices of the Royal Astronomical Society, 432, 336

Wright R. J., Lagos C. d. P., Davies L. J., Power C., Trayford J. W., Wong O. I., 2019, Monthly Notices of the Royal Astronomical Society, 487, 3740